The LENS Facilities and Experimental Studies to Evaluate the Modeling of Boundary Layer Transition, Shock/ Boundary Layer Interaction, Real Gas, Radiation and Plasma Phenomena in Contemporary CFD Codes

Michael S. Holden, PhD
CUBRC, Inc.
4455 Genesee Street
Buffalo, NY 14225, USA

holden@cubrc.org

1.0 OUTLINE

- The LENS Shock Tunnels and Expansion Tunnel Ground Test Facilities

- Studies of Boundary Layer Transition on Blunt and Slender Re-entry Vehicles

- Laminar and Turbulent Shock Interaction Studies

- Studies of Roughness and Blowing Effects on Blunt and Slender Hypersonic Vehicles

- Real Gas and Surface Catalysis Studies in the LENS I and XX Facilities

2.0 LENS SHOCK TUNNELS AND EXPANSION TUNNEL GROUND TEST FACILITIES

We operate five tunnels in the LENS supersonic and hypersonic ground test facility complex. The 48-inch shock tunnel was constructed in 1958 and represented one of the first facilities of its kind constructed to perform government and commercial testing at Mach numbers from 6 to 20. This facility has been used extensively to produce high-quality measurements in high Mach number, low Reynolds number flows where viscous interaction and rarefied gas phenomena are important. It has been used in the early capsule and space shuttle programs for NASA to collect design data for these systems. In the 50 years since it has been constructed, it has also been used in many studies to evaluate and improve the prediction methods used to design hypersonic vehicles. The LENS I facility was constructed in 1992 and used initially in programs to evaluate the aerothermal and aero-optical performance of hypersonic interceptors. Since then, it has been used in many studies to evaluate the aerothermal characteristics of re-entry vehicles and provide code validation data. The LENS II facility can be operated as a shock tunnel, Ludwieg tube and expansion tunnel. At the low Mach number end, it provides the capability to generate Reynolds numbers of the order of a billion while large-scale testing of full-scale hypersonic vehicles can be conducted at duplicated flight conditions up to Mach numbers of 10. With additional components, the LENS II tunnel can operate as an expansion tunnel which can generate velocities of up

Report Documentation Page

Form Approved
OMB No. 0704-0188

Public reporting burden for the collection of information is estimated to average 1 hour per response, including the time for reviewing instructions, searching existing data sources, gathering and maintaining the data needed, and completing and reviewing the collection of information. Send comments regarding this burden estimate or any other aspect of this collection of information, including suggestions for reducing this burden, to Washington Headquarters Services, Directorate for Information Operations and Reports, 1215 Jefferson Davis Highway, Suite 1204, Arlington VA 22202-4302. Respondents should be aware that notwithstanding any other provision of law, no person shall be subject to a penalty for failing to comply with a collection of information if it does not display a currently valid OMB control number.

1. REPORT DATE	2. REPORT TYPE	3. DATES COVERED
APR 2010	**N/A**	**-**

4. TITLE AND SUBTITLE	5a. CONTRACT NUMBER
The LENS Facilities and Experimental Studies to Evaluate the Modeling of Boundary Layer Transition, Shock/ Boundary Layer Interaction, Real Gas, Radiation and Plasma Phenomena in Contemporary CFD Codes	5b. GRANT NUMBER
	5c. PROGRAM ELEMENT NUMBER

6. AUTHOR(S)	5d. PROJECT NUMBER
	5e. TASK NUMBER
	5f. WORK UNIT NUMBER

7. PERFORMING ORGANIZATION NAME(S) AND ADDRESS(ES)	8. PERFORMING ORGANIZATION REPORT NUMBER
CUBRC, Inc. 4455 Genesee Street Buffalo, NY 14225, USA	

9. SPONSORING/MONITORING AGENCY NAME(S) AND ADDRESS(ES)	10. SPONSOR/MONITOR'S ACRONYM(S)
	11. SPONSOR/MONITOR'S REPORT NUMBER(S)

12. DISTRIBUTION/AVAILABILITY STATEMENT
Approved for public release, distribution unlimited

13. SUPPLEMENTARY NOTES
See also ADA569031. Aerothermodynamic Design, Review on Ground Testing and CFD (Conception aerothermodynamique, revue sur les essais au sol et dynamique des fluides informatisee).

14. ABSTRACT

15. SUBJECT TERMS

16. SECURITY CLASSIFICATION OF:			17. LIMITATION OF ABSTRACT	18. NUMBER OF PAGES	19a. NAME OF RESPONSIBLE PERSON
a. REPORT **unclassified**	b. ABSTRACT **unclassified**	c. THIS PAGE **unclassified**	**SAR**	**64**	

Standard Form 298 (Rev. 8-98)
Prescribed by ANSI Std Z39-18

to 20,000 ft/s. This facility was used as a prototype for the LENS XX facility which can operate with a hydrogen driver at higher pressure and temperature conditions to reach velocities of up to 30,000 ft/s. Figure 1 shows the velocity altitude capability of the LENS facilities and a list of hypersonic vehicles which, with the exception of Orbiter and Apollo capsule, have been tested at full-scale fully duplicated flight conditions.
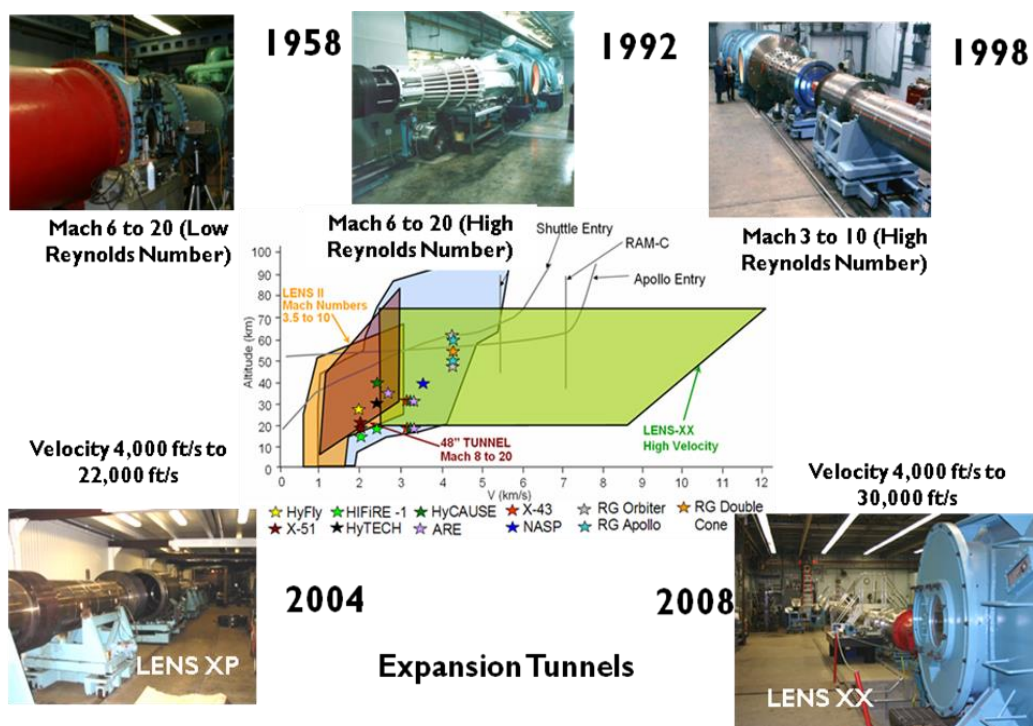

Figure 1: The LENS Shock and Expansion Test Facilities

The 48-inch tunnel has the capability to operate over a velocity range from 2,500 to 10,000 ft/s at unit Reynolds numbers from 1×10^5 to 5×10^7. Two contoured nozzles and a conical nozzle have been constructed and used on the 48-inch tunnel providing a Mach number range from 6 to 18 as shown in Figure 2. Fundamental measurements associated with shock/shock and shock/boundary layer interaction have been conducted in the 48-inch tunnel under fully laminar, transitional, and turbulent flow conditions. The shock/shock interaction studies have been conducted over cylindrical leading edges and on double cone configurations (see Figure 3) yielding measurements that have been extensively used to evaluate the modeling of viscous interaction phenomena associated with peak heating loads developed on hypersonic vehicles. Capsule studies have yielded wake flow measurements of the afterbody heating and we have used the high Mach number, low Reynolds number capability of the facility to study viscous interaction and rarefied gas phenomena on the heating loads and controllability of winged hypersonic vehicles.
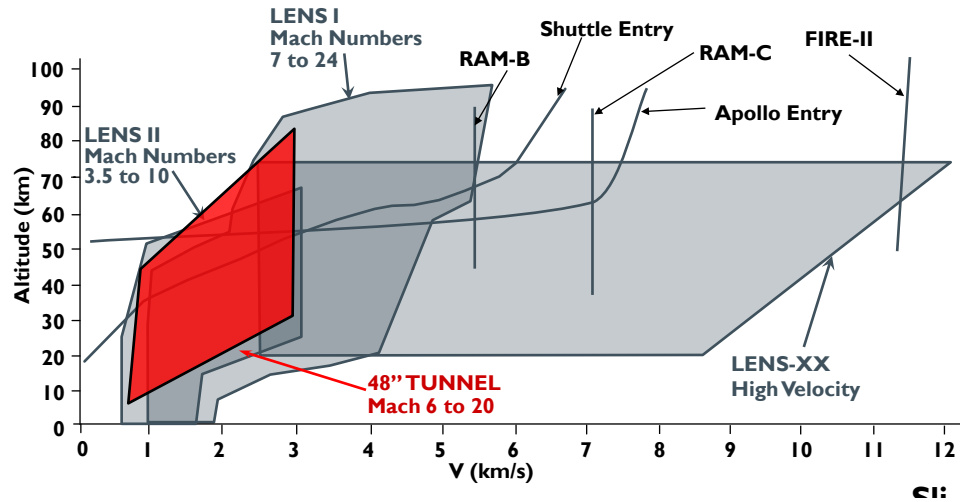
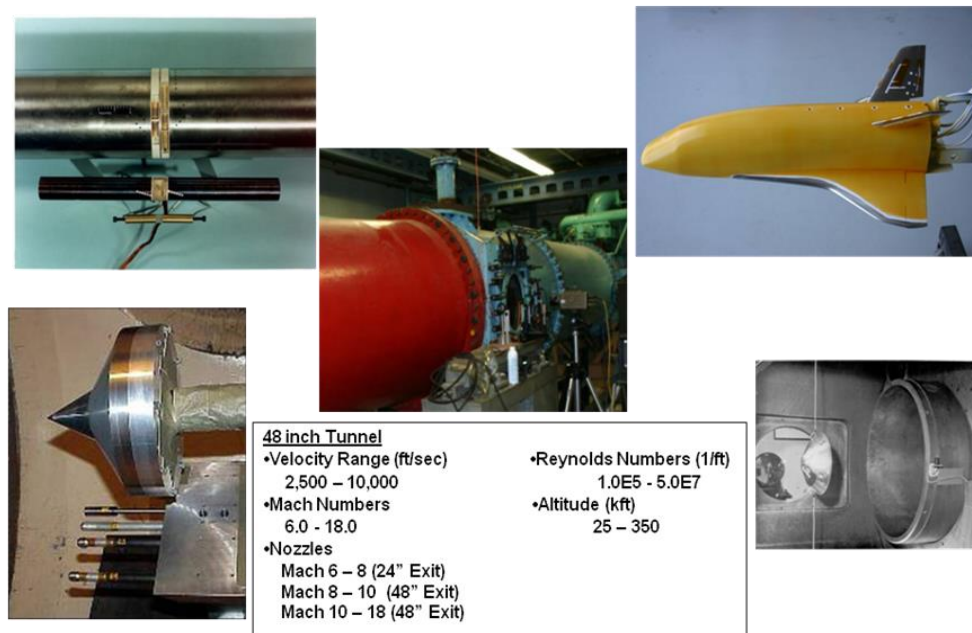Figure 2: Altitude/Velocity Map of the 48-Inch Shock Tunnel

Figure 3: 48-Inch Reflected Shock Tunnel – Key Facility for Low Reynolds Number Testing in Apollo and Space Shuttle Programs

Since its construction in 1992, LENS I has been used extensively to study a large range of aerothermal and aero-optical phenomena associated with the design of missiles, capsules, and scramjet propulsion vehicles. Three nozzles have been constructed for this facility, two of which are contoured and the third conical, which as shown in Figure 4, cover the Mach number range from 7 to 22.

Figure 4: LENS I Reflected Shock Tunnel – Atmospheric Re-entry and Flight for Earth and Planetary Re-entry (Mach 6 to 22)

Detailed measurements of the aerothermal loads on NASA's space shuttle and on other X-vehicles have been obtained with miniature surface instrumentation providing key data to evaluate the aerothermal design and provide data for code evaluation and validation. Recently, measurements have been made in support of new "inward turning" scramjet engine design concepts and to support the design and testing under the Air Force HIFiRE and Falcon programs. The LENS I facility has a unique capability to evaluate viscous interaction and real gas phenomena over hypersonic vehicles in the high Mach number, low Reynolds number range as illustrated in Figure 5. Models up to 18 ft long and 4 ft in diameter have been used in scramjet and capsule studies respectively to duplicate the high-temperature high-Reynolds number conditions (see Figure 6) where boundary layer transition and flow chemistry are important on these vehicles.
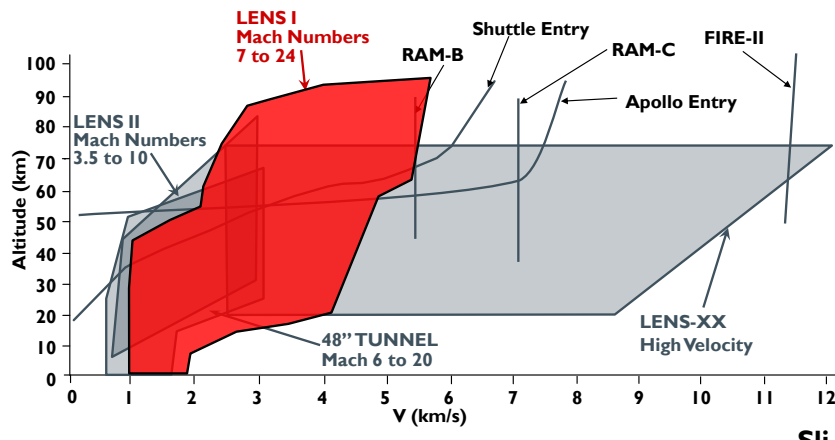
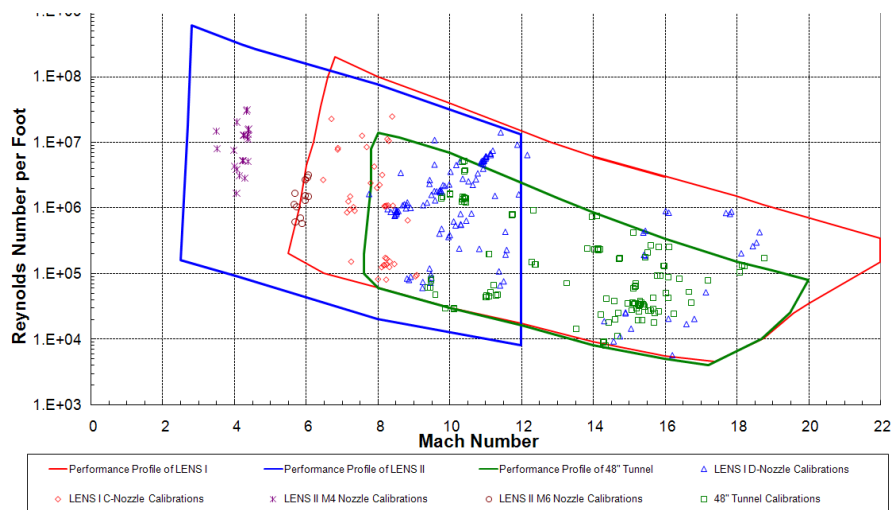**Figure 5: Altitude/Velocity Map of the LENS I Facility**

Figure 6: Mach Number/Reynolds Number Simulation Map of the LENS Facility

The LENS II facility shown in Figure 7 was constructed specifically to perform high Reynolds number studies in supersonic and hypersonic flows on large-or full-scale replicas of flight vehicles. Four nozzles, three contoured and the fourth conical, have been constructed for this facility to enable us to test from Mach 2.7 to 10 at maximum Reynolds numbers close to 1 billion (as shown in Figure 8). The velocity/altitude map for this facility is shown in Figure 9. We have conducted full-scale testing at fully duplicated flight conditions with interceptor and scramjet-powered vehicles. We have also tested the shuttle stack at duplicated Mach number, Reynolds number and velocity conditions as shown in Figure 7.
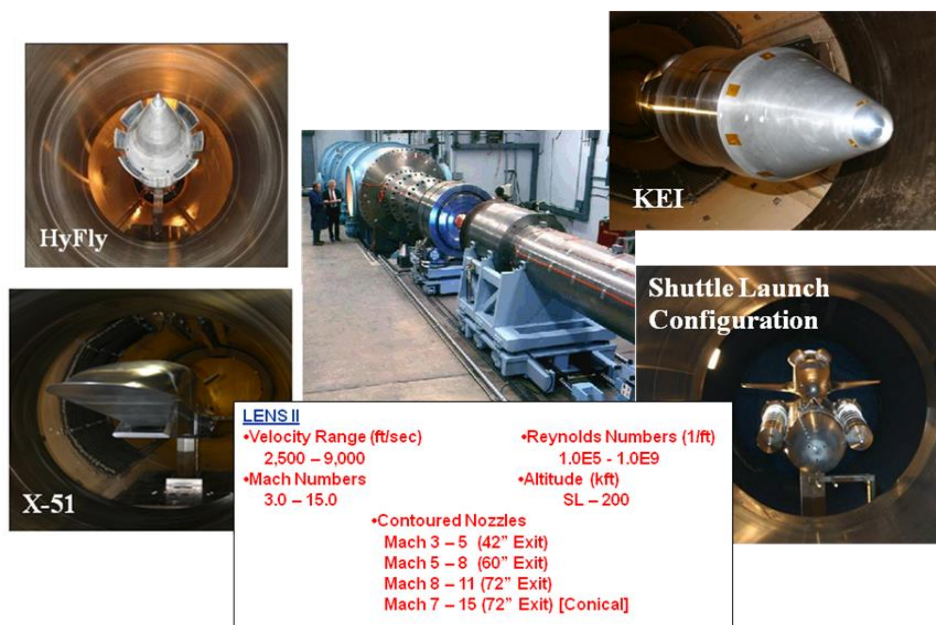
Figure 7: LENS II Reflected Shock/Ludweig Tunnel – High Reynolds Numbers, Large-scale Models, Perform Critical Path Testing for NASA (Mach 3 to 10)

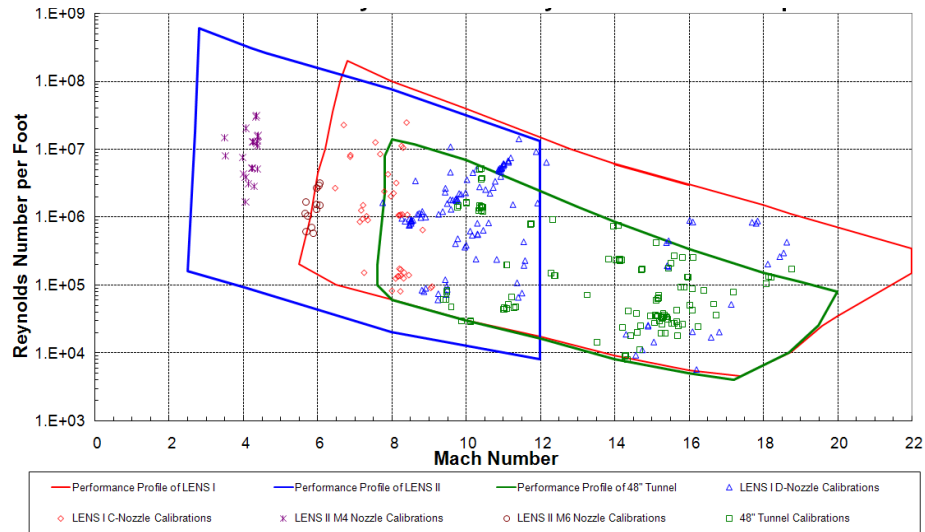**Figure 8: Mach/Reynolds Number Capability of LENS II**
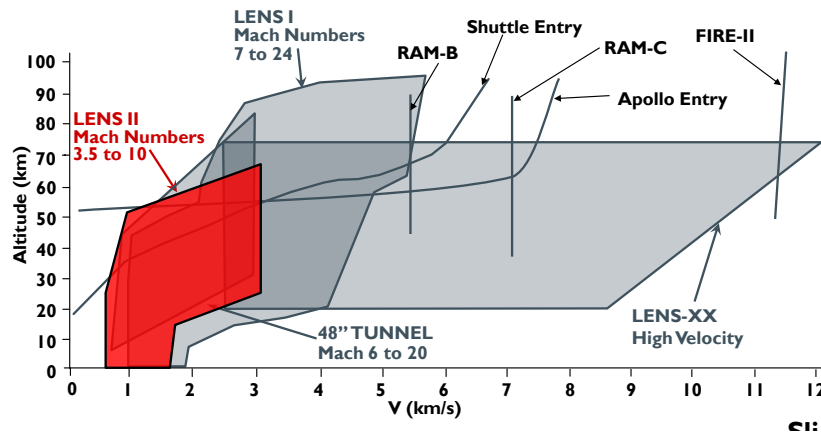

Figure 9: Altitude/Velocity Map of LENS II Facility

The 48-inch tunnel and the LENS I and II facilities are principally operated as reflected shock tunnels. The incident shock which is used to compress the test gas is generated by the sudden release of the driver gas by rupturing a pair of diaphragms contained in a double diaphragm assembly shown in Figure 10. The incident shock is reflected at the end wall of the driven tube; it produces a high-temperature high-pressure reservoir of gas which is expanded isentropically into the test section. The test time is limited by the appearance of the driver gas when it moves through the nozzle behind the contact surface between the hot driver gas and the heated test gas. Typically test times from 5 ms to 50 ms are generated in this way giving flow lengths which can be as long as 100 times the diameter of the capsule providing steady laminar and turbulent flows in the wake.
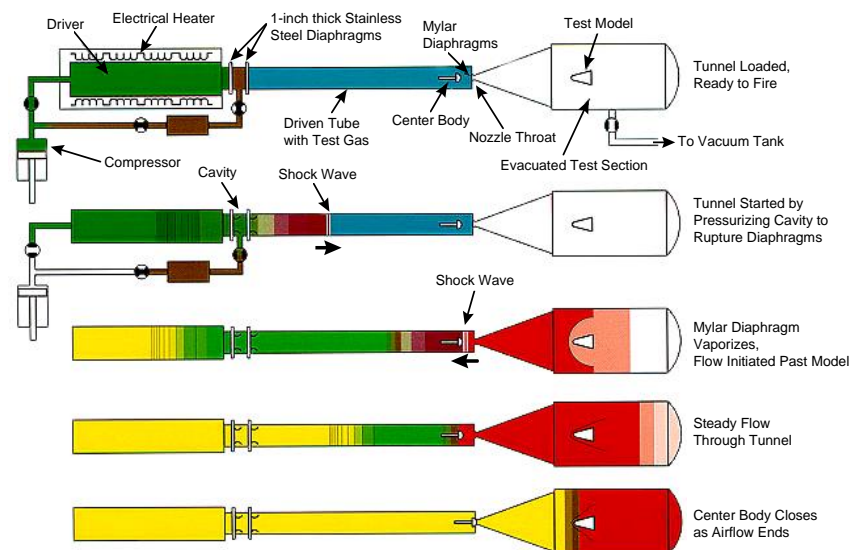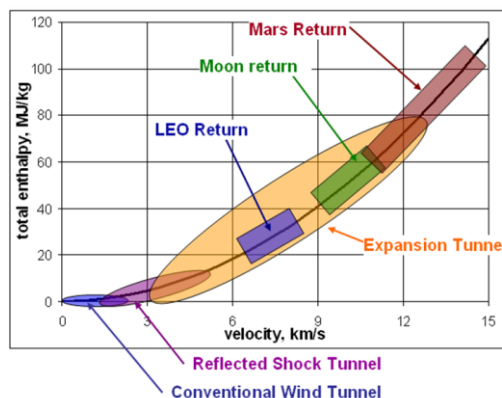
Figure 10: Schematic Diagram of the Operation of a Reflected Shock Tunnel

- Conventional facilities do **NOT** generate the enthalpy levels necessary to replicate the physics of reentry
- Reflected shock tunnels and arcjets generate reactive flows but at the price of uncertainties in the properties of the freestream state
- The expansion tunnel is the most effective capability to generate a high enthalpy flow that is clean and quiescent like that of flight.

Figure 11: Requirements to Duplicate High-enthalpy Flows over Re-entry Vehicles

LENS X and LENS XX are both expansion tunnels initiated when it was clear that it was difficult to characterize nonequilibrium properties of the test gas developed when testing at total enthalpies above the 5 MJ/kg to 8 MJ/kg range. As shown in Figure 11, the generation of clean air at enthalpies typical of return from low earth orbit, requires total enthalpies of above 20 MJ/kg and return from lunar and Martian orbits requires enthalpies above 60 MJ/kg. Currently, we believe such conditions can be achieved only in large expansion tunnels. In the expansion tunnel the test gas is heated and accelerated by a shock wave and an unsteady expansion as illustrated in Figure 12. The test gas which is placed in the driven tube is heated by a single shock bringing the temperature to below the value where NO

formation begins. This test gas is then accelerated through an unsteady expansion in the acceleration tube, generating a gas at atmospheric temperatures which can be accelerated to velocities of up to 30,000 ft/s. For large-scale facilities such as LENS X and LENS XX, we can generate test times typically 2 ms across a range of high enthalpies. The flow in the acceleration tube is expanded isentropically in the test section to give flow lengths of over 200 ft or 100 base diameters of a 1-ft test article; clearly long enough to establish the flow over the forebody and in the near wake. Figure 13 shows a photograph of the LENS XX facility and the range of test conditions over which it will be operated. We expect to achieve test times of up to 4 ms; we have used a conical nozzle to expand the flow into the test section of our expansion tunnel. The velocity altitude range projected for the LENS XX is shown in Figure 14. The major emphasis for the testing in the LENS XX will be to evaluate real gas and radiation effects. Our near-term objectives will be to obtain measurements to replicate those obtained in the Fire II and BSUV flight experiments to supply information with which to develop more sophisticated models of air chemistry at total enthalpy levels of greater than 10 MJ/kg.
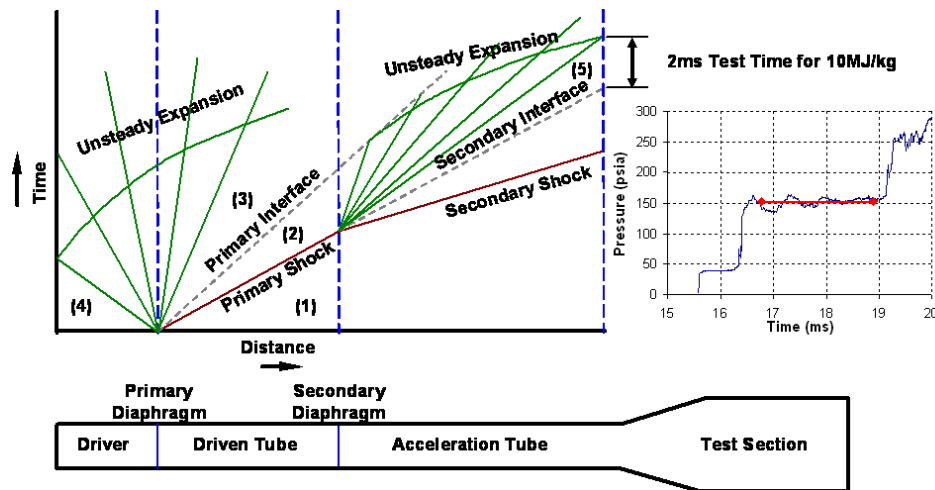

Figure 12: Wave Diagram of LENS XX Expansion Tunnel

Figure 13: Capabilities of LENS XX Expansion Tunnel Facility
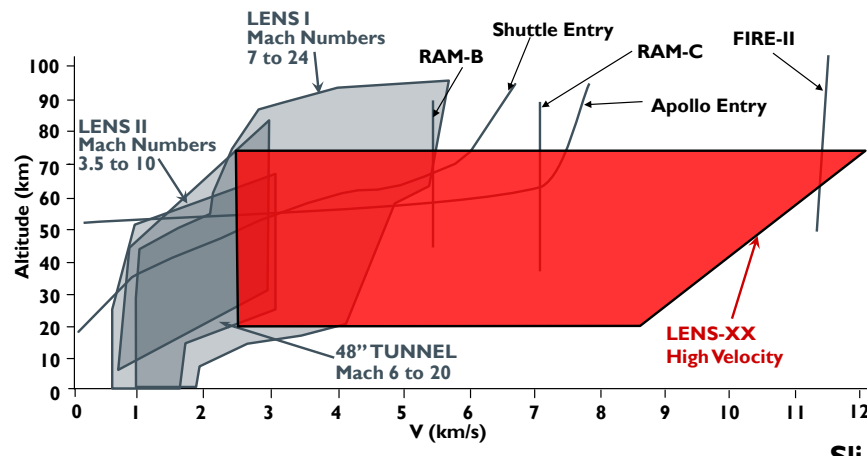
Figure 14: Velocity/Altitude Capability of LENS XX

3.0   STUDIES OF BOUNDARY LAYER TRANSITION ON BLUNT AND SLENDER RE-ENTRY VEHICLES

The overall objective of the work conducted in the LENS facilities is to provide techniques to predict boundary layer transition on flight vehicles from measurements in the LENS tunnels conducted at duplicated flight conditions on full-scale test articles. The basic approach illustrated in Figure 15 will be to obtain measurements of transition in the tunnels duplicating the conditions encountered in a specific flight test, for example, the measurements of transition obtained on the X-43 configuration. At these conditions, we will obtain measurements of the disturbance levels in the tunnel using high-frequency pressure and hot-wire/film instrumentation (see Figure 16). From these ground test measurements we will extrapolate to flight using the STABL code developed by the University of Minnesota as well as the more recently developed transition prediction technique based on direct numerical simulation, also developed by the University of Minnesota. Combining flight data, ground test duplicated conditions, measurements of freestream disturbance levels, and numerical extrapolation techniques will result in a more rational method than currently exists to predict boundary layer transition on flight vehicles from ground test data. Currently we have made transition measurements in the LENS facilities on full-scale replicas of the X-51, HyFly and HIFiRE 1 and 5 configurations illustrated in Figure 17 and are planning to obtain similar transition data on the X-43, HIFiRE 2 and the Re-Entry F Flight Tests. We plan to obtain measurements of the freestream disturbance levels in the LENS I and II facilities at freestream conditions which will duplicate those obtained in flight. Combining all these results we plan to develop a more rational approach to predict transition in flight from ground test data and numerical analysis.

Existing Flight Data

Ground Tests of Full-scale Vehicles at Flight Conditions

Flight Transition Prediction Tool from Ground Test Measurements at Duplicated Vel/Alt Conditions

Freesteam Pitot Pressure Fluctuations

Disturbance measurements in the flowfield and on the surface

Surface Pressure Fluctuation Frequencies

University of Minnesota
• *STABL [2D and 3D]*
• *Direct Numerical Simulation [DNS]*
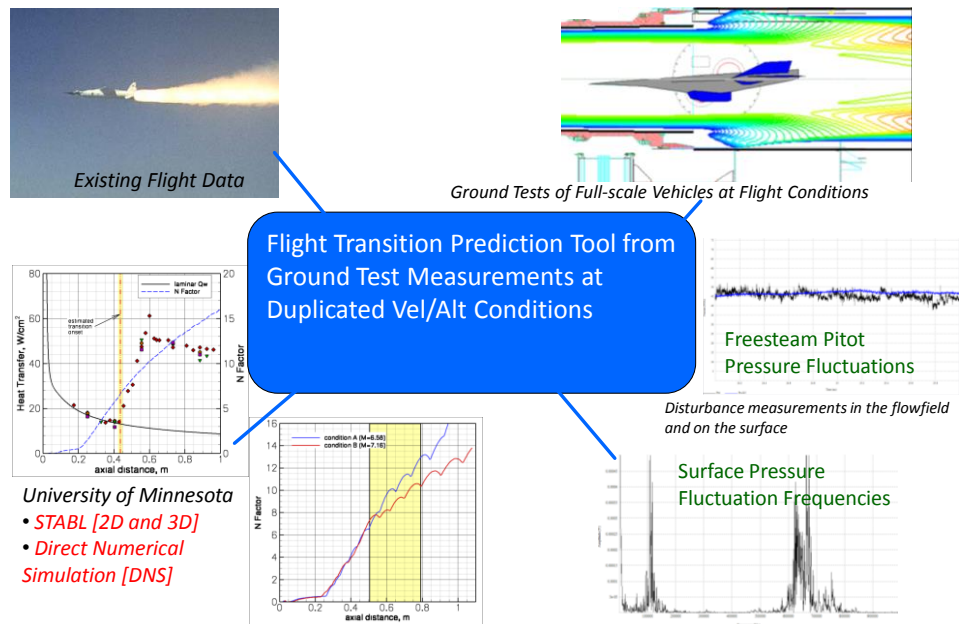
Figure 15: Develop Validated Numerical Analysis Techniques to Predict Boundary Layer Transition from Ground Test Measurements at Duplicated Flight Conditions

Flowfield Measurements
• Intrusive
    • Hot Wires
    • Hot Films
    • Thin-film
    • Pitot Pressure
• Non-intrusive
    • Laser Absorption Differential Velocimetry
    • Spatial Laser Differential Interferometry
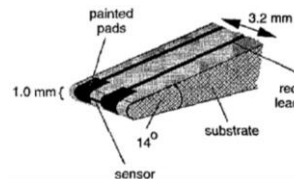
Surface Measurements
• Thin-film
• Pressure Sensors
    • PCB Piezoelectric
    • Fiber Optics/MEMS
    • Kulite Piezoresistive
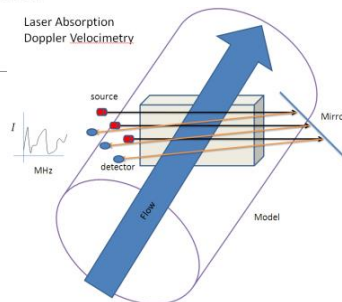
Figure 16: Measurement Techniques to Evaluate Facility Disturbance Environment
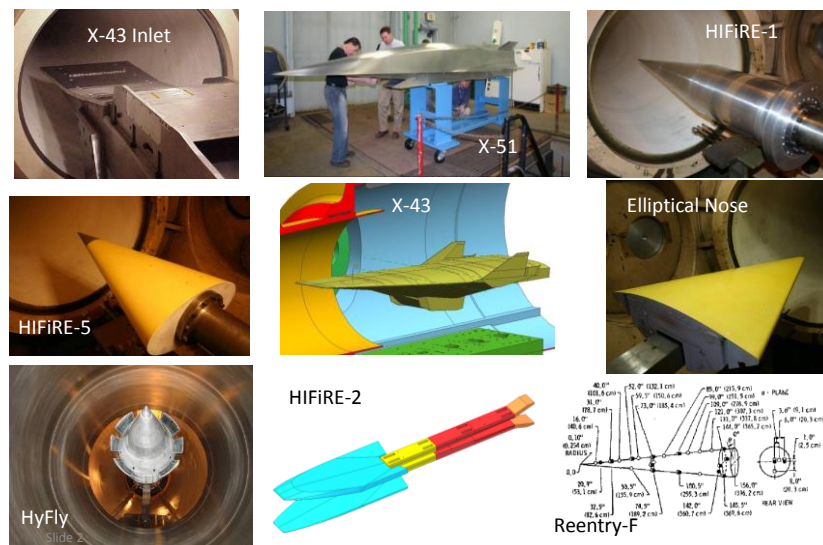
Figure 17: Transition in Hypervelocity Flows: CUBRC Focus – Fully Duplicated Ground Test Comparisons

In the HIFiRE-1 program, we have performed detailed experimental studies and computations to optimize the design of the vehicle (a cone/cylinder flare model) to provide ground-to-flight comparisons of boundary layer transition, shock boundary layer interaction, and inlet mass capture as outlined in Figure 18. The models and instrumentation used in the ground test studies conducted in the LENS I facility are illustrated in Figure 19. Because the flare on the flight test article was too short to provide well-defined boundary conditions for the computations, we made additional measurements on a longer flare where the boundary layer downstream of reattachment was of sufficient length to generate a constant pressure well-defined boundary layer. Comparisons between simple prediction methods and measurements on the cone and cylinder section of the model are shown in Figure 20. The heat transfer measurements were in good agreement with the Cheng laminar prediction and the turbulent prediction of Van Driest II.
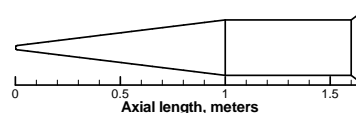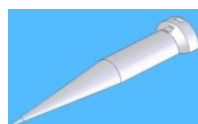
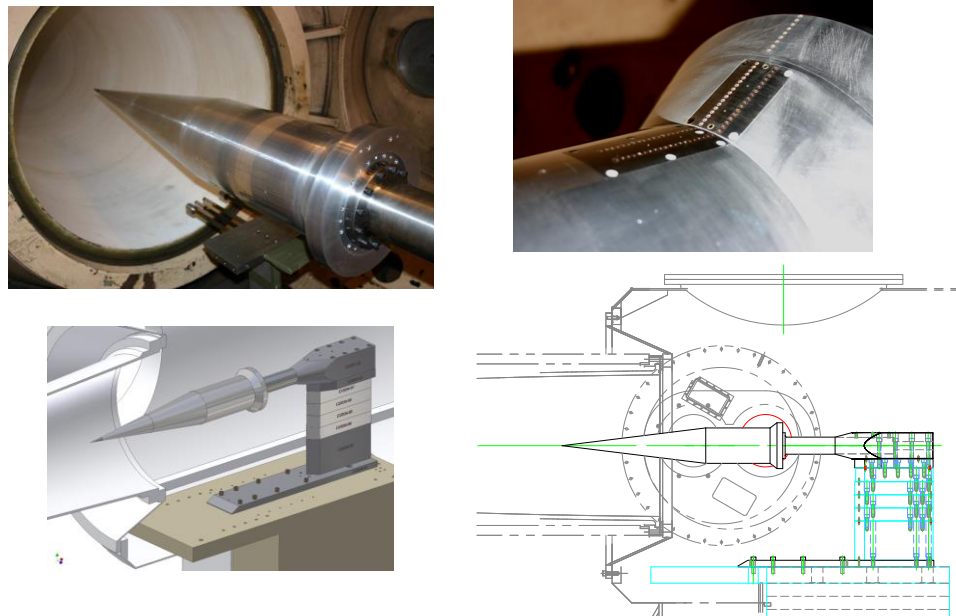**Figure 18: HIFiRE-1 Program Objectives and Experimental Background**

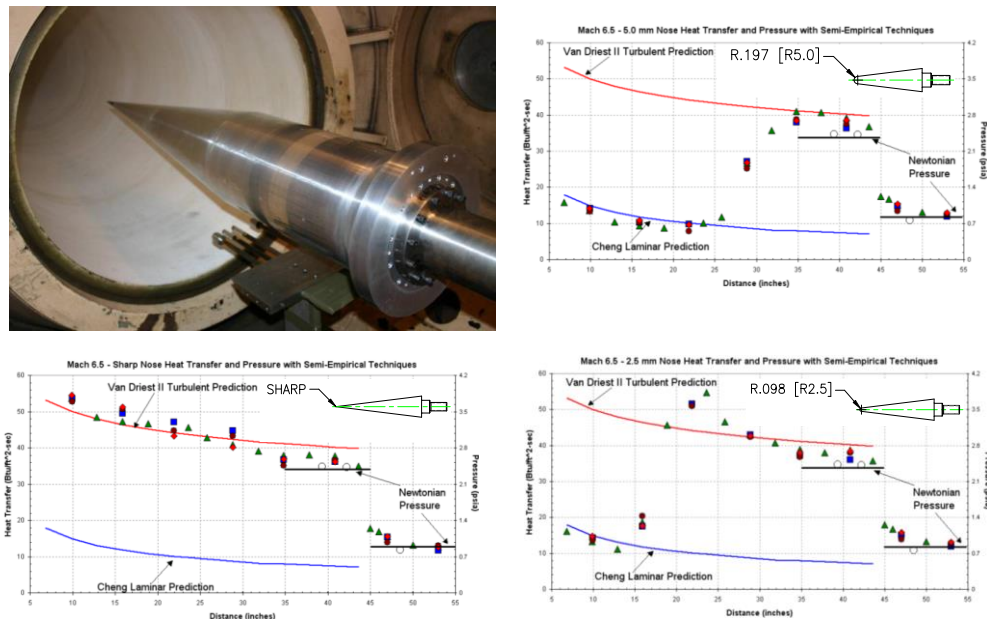**Figure 19: Full-scale HIFiRE-1 Model Installed in LENS 1**

Figure 20: Full-scale HIFiRE-1 Geometry Selection Studies at Duplicated Mach 6 and 7 Flight Conditions

In the HIFiRE Program, we employed miniature thin-film instrumentation and high-frequency pressure gages (see Figure 21) to track the disturbances that are created during the transition process. Figure 22 shows a Schlieren photograph of a transitioning boundary layer along the forebody of the HIFiRE vehicle. The heat transfer record from a thin-film gage at station 1 illustrates the intermittent nature of the transition process and at this particular point in time the flow is laminar over gage 1. As the

disturbances travel downstream, the region of laminar flow decreases in size and by gage 2, the flow is turbulent at least 50% of the time. Gages 3 and 4 are situated at the end of the transition process and it can be seen that, from the gage output, the flow is almost completely turbulent over the cone at Station 4.
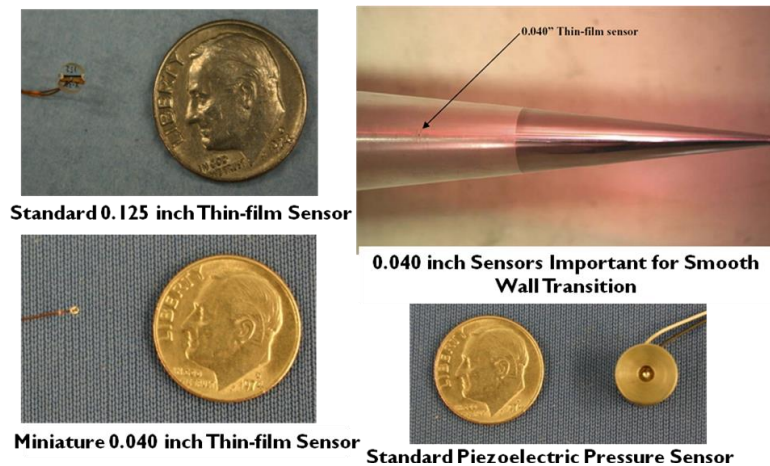

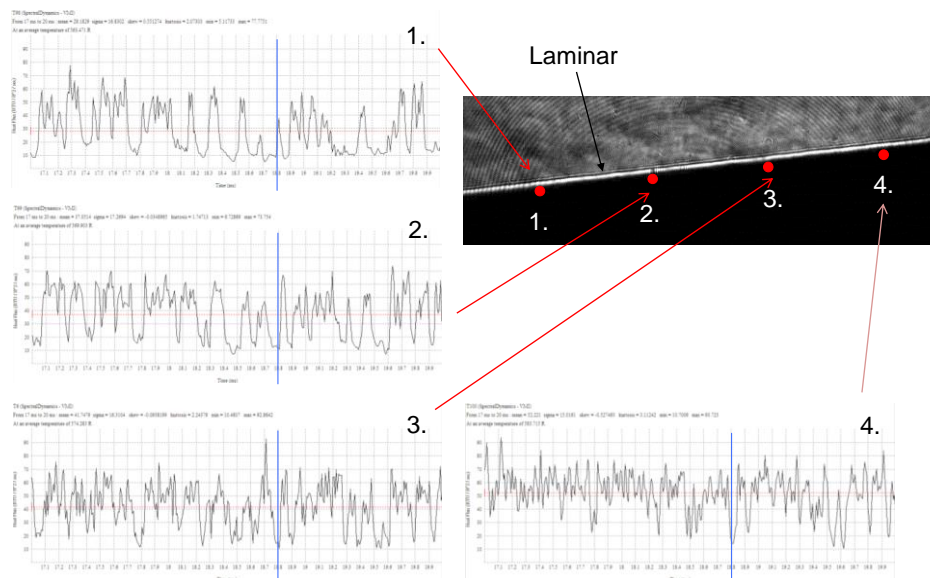**Figure 21: HIFiRE-1 Heat Transfer and Pressure Instrumentation**

Figure 22: HIFiRE-1 Schlieren showing Laminar Boundary Layer compared to Time History Traces
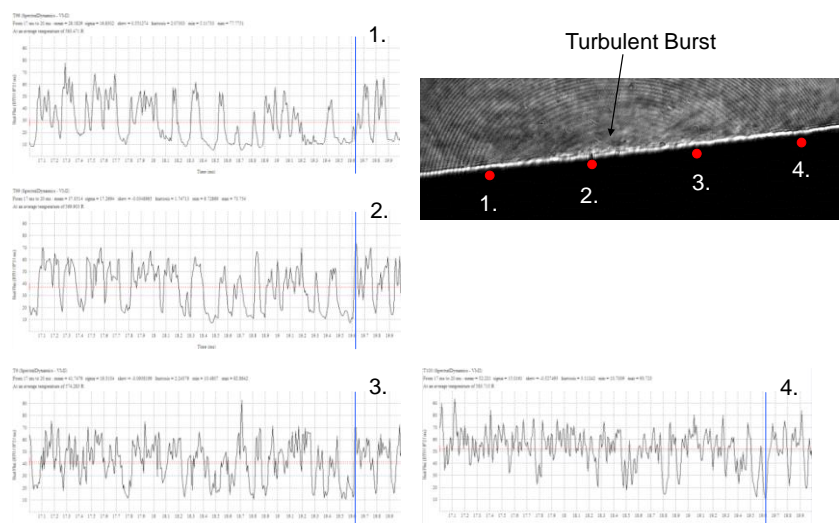
Figure 23: Typical Transition Data in the LENS Facility over the 7.0° HIFiRE Cone Showing Turbulent Bursts

Figure 23 shows a Schlieren photograph and heat transfer records illustrating a turbulent burst which traverses the length of the cone at just less than freestream velocity. These turbulent bursts are observed at Reynolds numbers slightly less than those at which a well-defined transition region is established over the cone. Again the heat transfer records illustrate that instantaneously, both in front and behind the turbulent burst, are regions of laminar flow. The Schlieren photograph of a well-established transition region is shown in Figure 24. Here we see the "rope wave" instabilities which precede the formation of large scale instabilities that grow as they move downstream, eventually dissipating into smaller scale turbulence toward the end of the transition process.
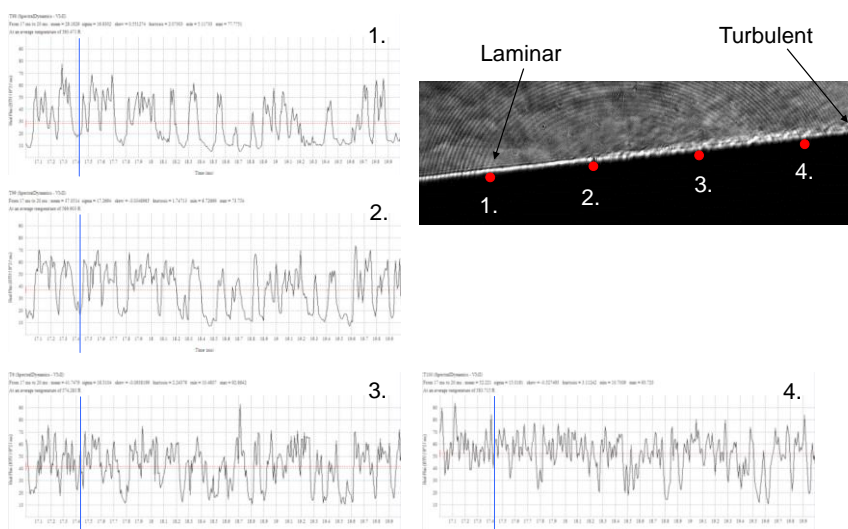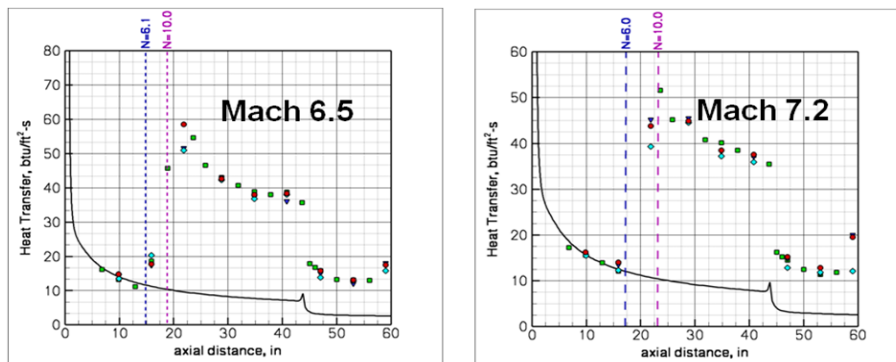

Figure 24: Schlieren from HIFiRE Program compared to Individual Heat Transfer Time Histories

- Assuming N_{FLIGHT}=10 pushes transition back by ~ 4-5".
- This is still further forward than we measured with the larger nose radius(5.0-mm).
- The larger nose radius stayed turbulent beyond the expansion corner, so we conclude that the 2.5-mm radius should produce turbulent flow in the interaction region in flight.
- More detail concerning this process can be found in MacLean AIAA 2007-4490

Figure 25: Entry 1 Computational Results and Stability Analysis to Extrapolate Transition Point to Flight

Figure 25 shows comparisons between the measurements of heat transfer in the transition region over the conical forebody for both the Mach 6.5 and 7.2 flight conditions. We see that transition begins at approximately 15 inches from the cone tip at the Mach 6.5 condition and is completed at the 22 inch axial station. The n factors from experiment in these studies varied between 6 and 6.5 and it can be seen that for an n factor of 10, which is considered typical for flight data, transition would be delayed by approximately 4 to 5 inches, which is in fact where the region of turbulent overshoot occurs on the cone. Similar measurements at Mach 7.2 are also shown in this figure and we again see transition overshoot occurs at the streamwise station where the STABL code predicts the beginning of transition. If the results from the STABL code are to be believed, tunnel noise results in only a small forward movement of the transition region relative to the overall transition length.
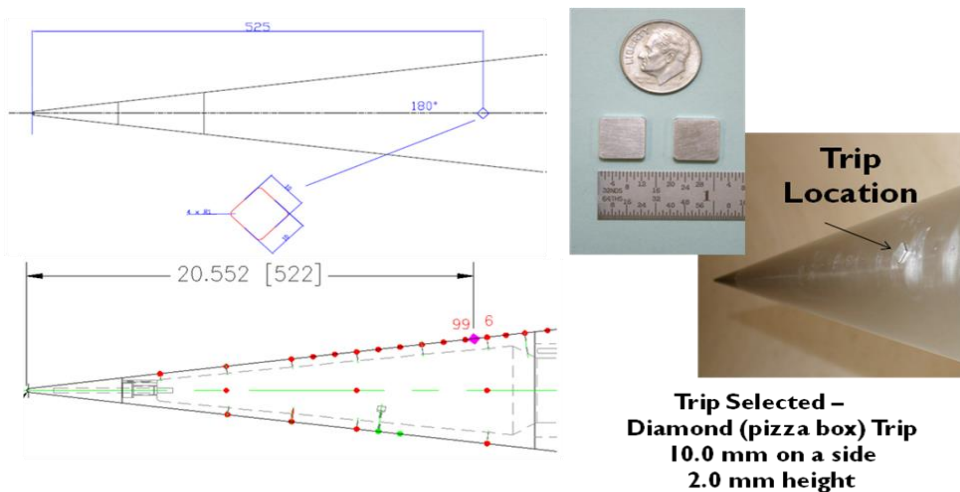

Figure 26: Single Side Tripping to Obtain Turbulent Flow over an Extended Time in Flight

During the ground test program to study the HIFiRE configuration, measurements were also made to design trips to be placed on the conical forebody to induce transition in wedge-shaped regions along the cone. Figure 26 shows the geometry of the "pizza box" trips and their location on the conical forebody. Measurements of heat transfer made in these studies are shown in Figure 27, illustrating that the trips worked effectively and can be used to develop turbulent boundary layers over the conical forebody and cylindrical section of the model preceding the conical flare. Measurements suggest that the boundary layer remains fully turbulent through the expansion fan at the cone/cylinder junction and that the interaction region at the cylinder/flare junction is completely turbulent.
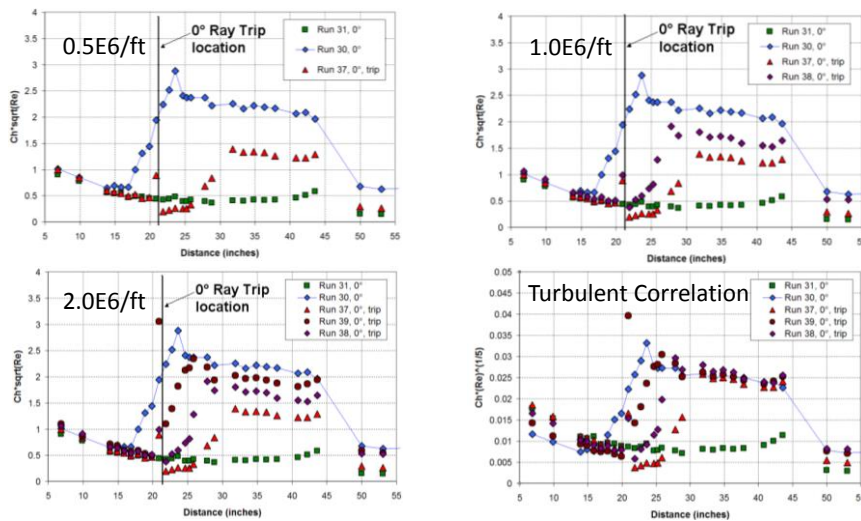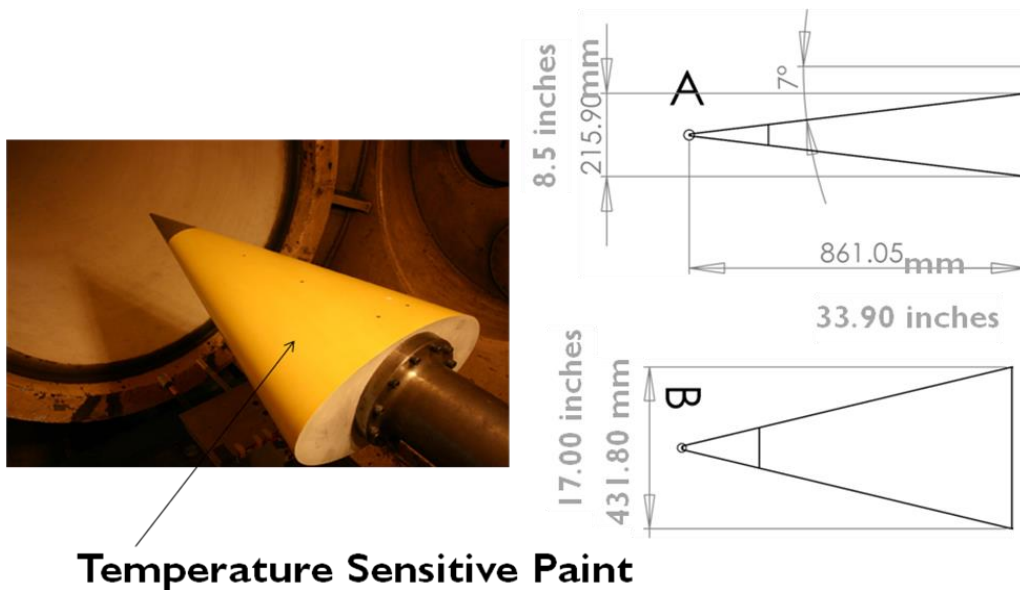

Figure 27: Cone Section Heat Transfer Results with Single Trip over Range of Reynolds Numbers

Figure 28: Full-scale Elliptic Cone Model for HIFiRE-5 Studies

Measurements were also made on a full-scale replica of the HIFiRE 5 configuration, which is a blunted elliptical cone configuration shown in Figure 28. The transition measurements on this configuration were made principally with temperature-sensitive paint to capture the three-dimensional structure of the crossflow-induced transition regions developed on the leeside of the cone. Records from the temperature-sensitive paint shown in Figure 29 illustrate the three-dimensional nature of the transition process which has developed on the leeside of the cone at angle of attack. Also shown in Figures 30 and 31, we see temperature-sensitive paint records illustrating the boundary layer transition on the attachment line of the HIFiRE 5 configuration. Measurements of both cross flow and attachment line transition suggest that the original conditions selected for the flight should be modified to achieve larger regions of laminar and transitional flows of greater use to the development and evaluation of methods for predicting transition.
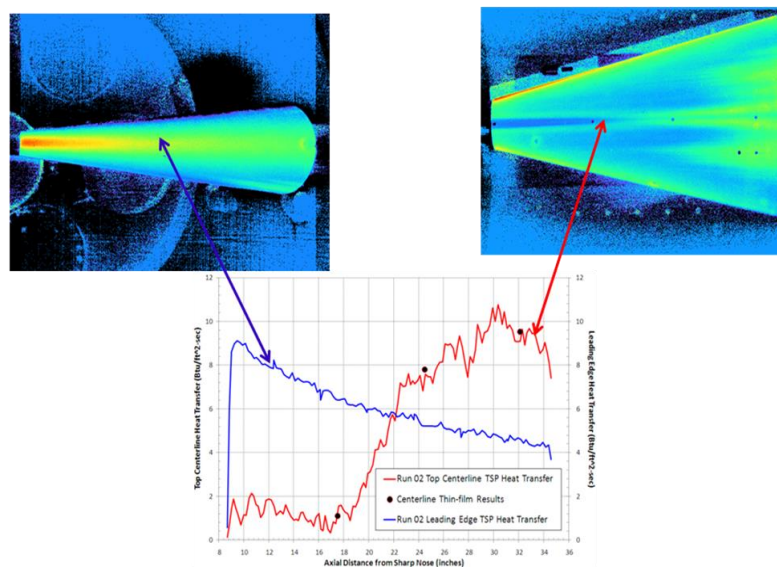

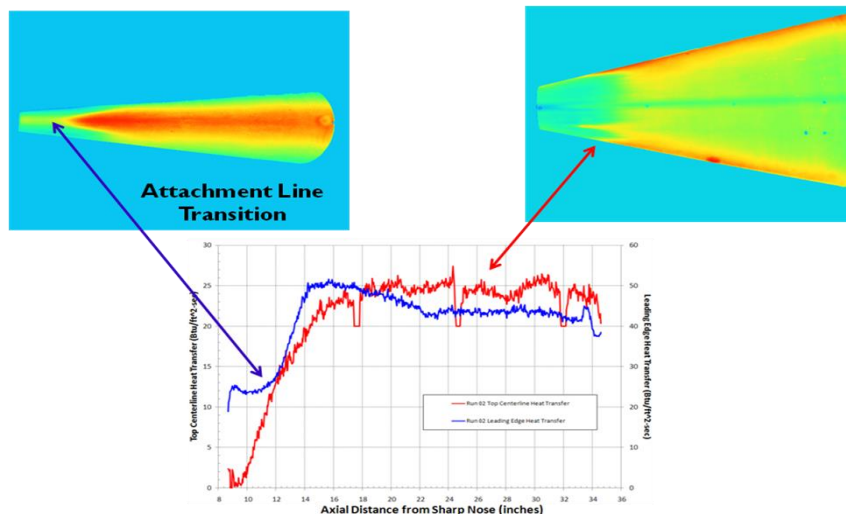**Figure 29: Transition at High Altitude (Test Point 1) on Leading Edge and Frustum of HIFiRE 5 Elliptic Cone**

Figure 30: Transition at Mid-altitude (Test Point 2) on Leading Edge and Frustum of HIFiRE 5 Elliptic Cone
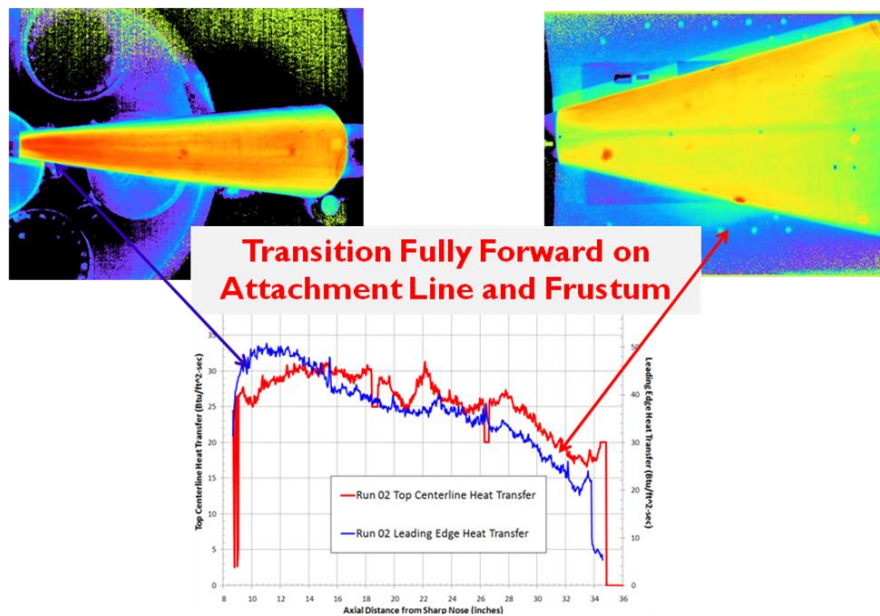
Figure 31: Transition at Low Altitude (Test Point 3) on Leading Edge on Frustum of HIFiRE 5 Elliptic Cone

Comparisons between measurements with the temperature-sensitive paint and thin-film instrumentation shown in Figure 32 demonstrates that the temperature-sensitive paint gives heat transfer values which are very close to the time-averaged value of the thin-film data in the transition regions of the flow.
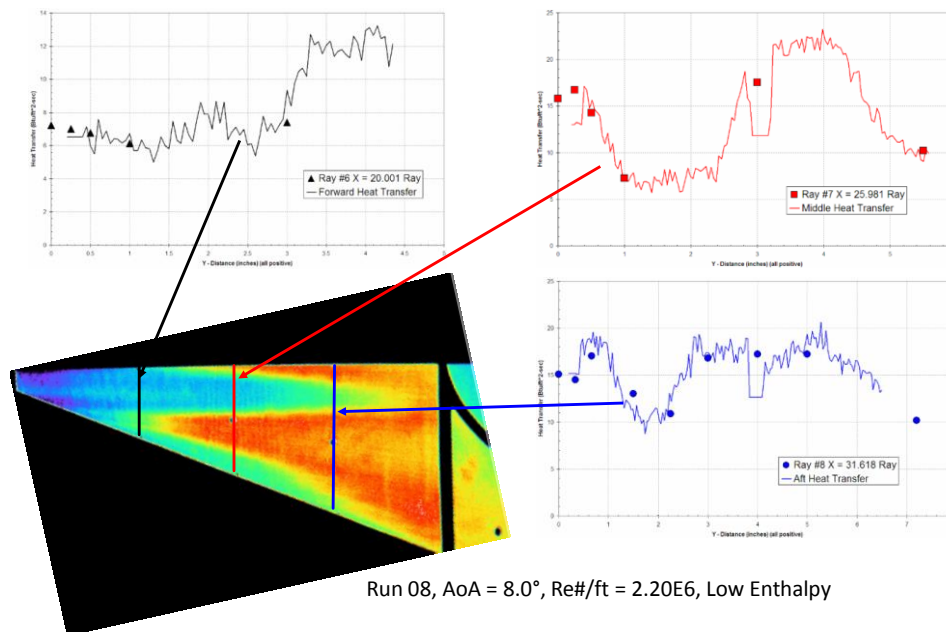

Run 08, AoA = 8.0°, Re#/ft = 2.20E6, Low Enthalpy

Figure 32: Transition Front Behavior for Reynolds Number Sweep at Mach 14

Trip-development studies with the full-scale HyFly vehicle (shown in Figure 33) at the Mach 6 flight condition resulted in a successful trip design where the values of heating downstream of the trip did not exceed those to a fully turbulent boundary layer at that station. For studies at the highest Reynolds number condition where boundary layer trips did not produce turbulent flow, our measurements indicated that transition occurred at n factors between 6 and 7 in a wind tunnel flow and we would expect boundary layer transition to occur on the nosetip of the flight vehicle just downstream of the trip.
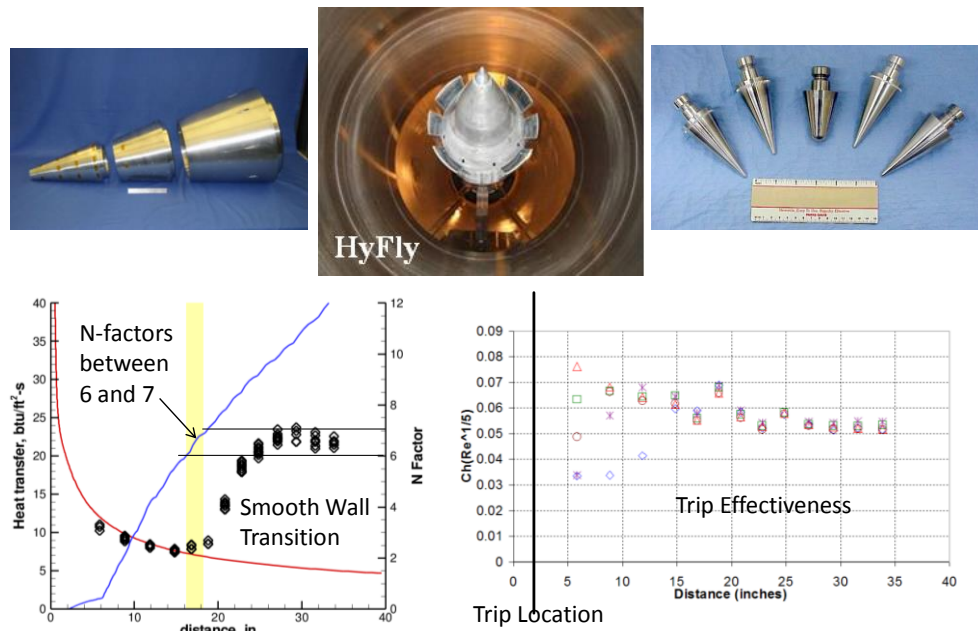

Figure 33: Studies of Smooth Body and Tripped Transition on Full-scale HyFly Vehicle at Mach 6 Flight Conditions

Aerothermal measurements were also made on a full-scale replica of the X-51 configuration tested at duplicated flight conditions.   A typical set of measurements obtained on the compression ramp of the X-51 inlet are shown for both tripped and untripped configurations in Figure 34. Here we see that the trips are effective in showing that the blowing in the inlet to this configuration to be fully turbulent at typical flight conditions.
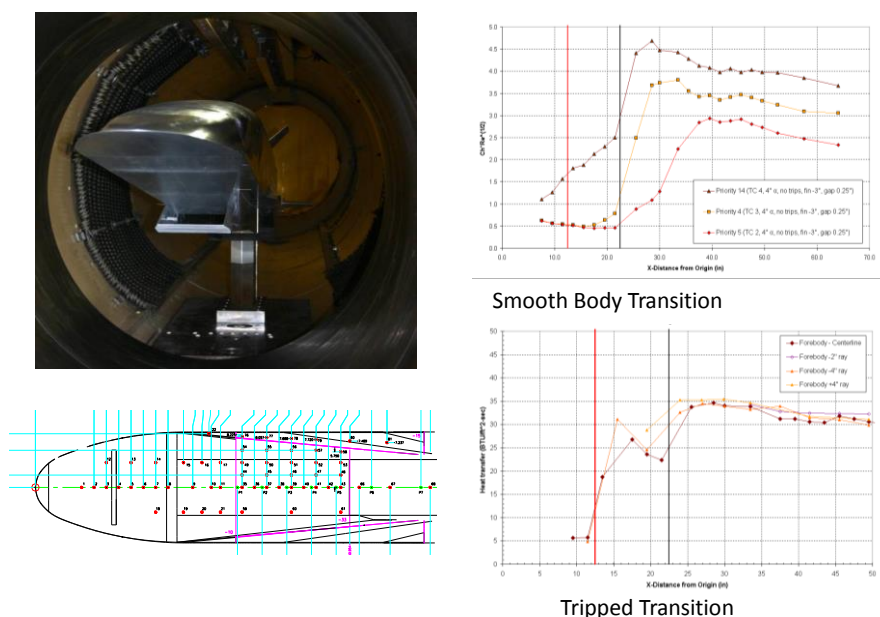
Smooth Body Transition

Tripped Transition

Figure 34: Full-scale X-51 Aerothermal Studies at Duplicated Flight Conditions: Smooth Body and Tripped Forebody Transition

Comparisons were also made with measurements made by Purdue in subscale tests of the inlet ramp of the X-51 configuration which are shown in Figures 35 and 36. In the Purdue studies, the tunnel was run under "quiet" and "noisy" conditions and the results shown in Figures 35 and 36 show a significant forward movement of transition when the throat region of the flow in the Purdue tunnel produces a noisy environment with an unsteady transitional flow on the tunnel walls. CUBRC's measurements in a conventional tunnel show transition occurs slightly ahead of the transition point in Purdue's tunnel run in the quiet mode. However, we see that in both facilities the flow is fully turbulent at close to the same downstream Reynolds number. We conclude that the noise level in the LENS II shock tunnel in which the studies were conducted does not significantly influence the location beginning and end of the transition region.
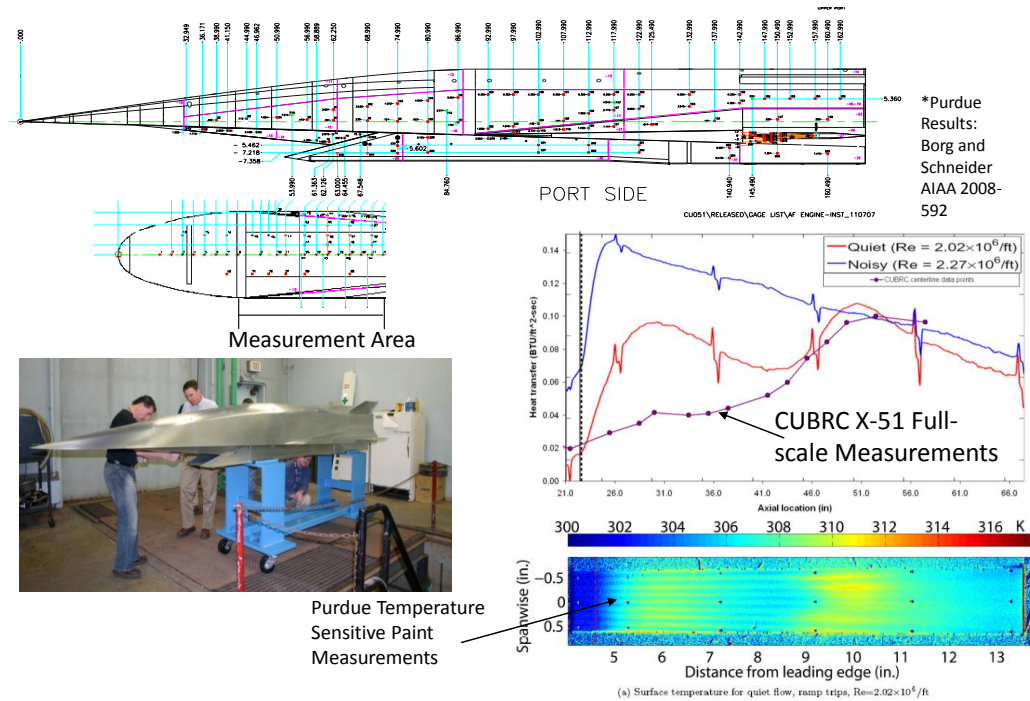
Figure 35: Full-scale X-51 Aerothermal Studies at Duplicated Flight Conditions – Comparisons with Purdue Results
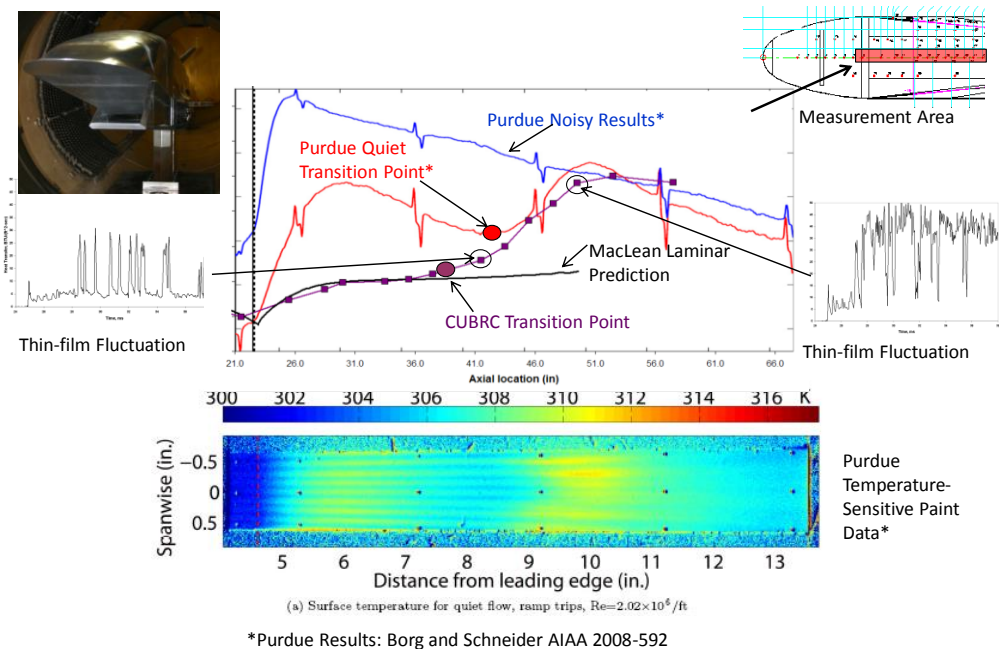

Figure 36: Tripped Transition Measurements in LENS II compared with Data from Purdue Quiet Facility

Transition measurements have also been made in the LENS 1 tunnel to study the transition process with tripped and untripped configurations of the X-43 inlet. A major objective of these studies was to determine the effect of tripping and transition on the heating loads to the cowl inlet (see Figure 37). However, measurements were made which can be compared directly with measurements made in flight. Measurements of boundary layer transition on the upper surface of the X-43 were obtained during flight at Mach 7 and 10 as illustrated in Figure 38, and we plan to test a full-scale replica of the X-43 (see Figure 39) in the LENS facility at duplicated flight conditions between Mach 5 and 7. Measurements will be made with high-frequency pressure and thin-film sensors, the locations of which are shown in Figure 40, and temperature-sensitive paint will be used to investigate potential crossflow transition phenomena.
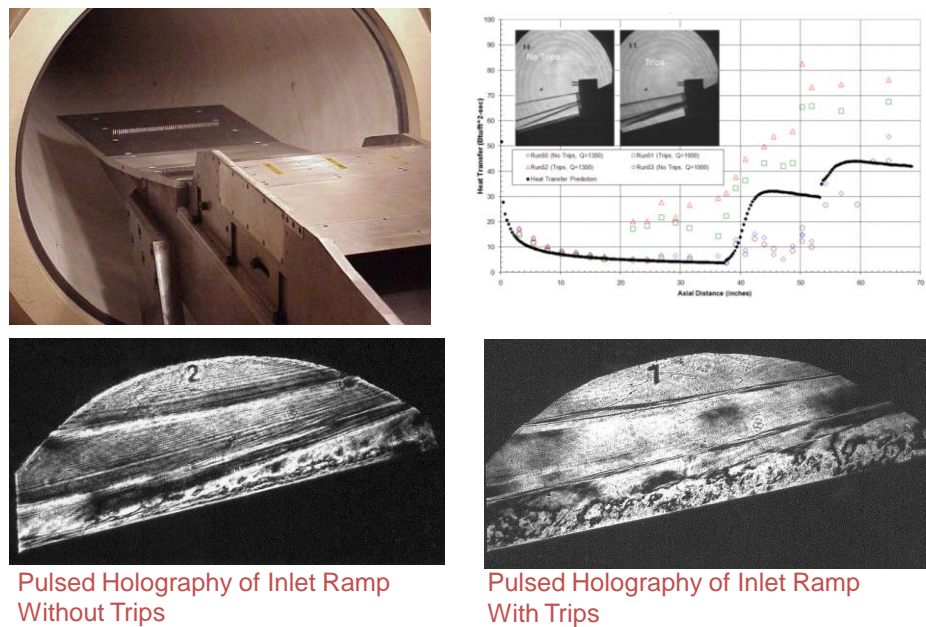

Pulsed Holography of Inlet Ramp Without Trips

Pulsed Holography of Inlet Ramp With Trips

Figure 37: X-43 Full-scale Engine Flowpath Testing and Comparison to Flight Boundary Layer Transition
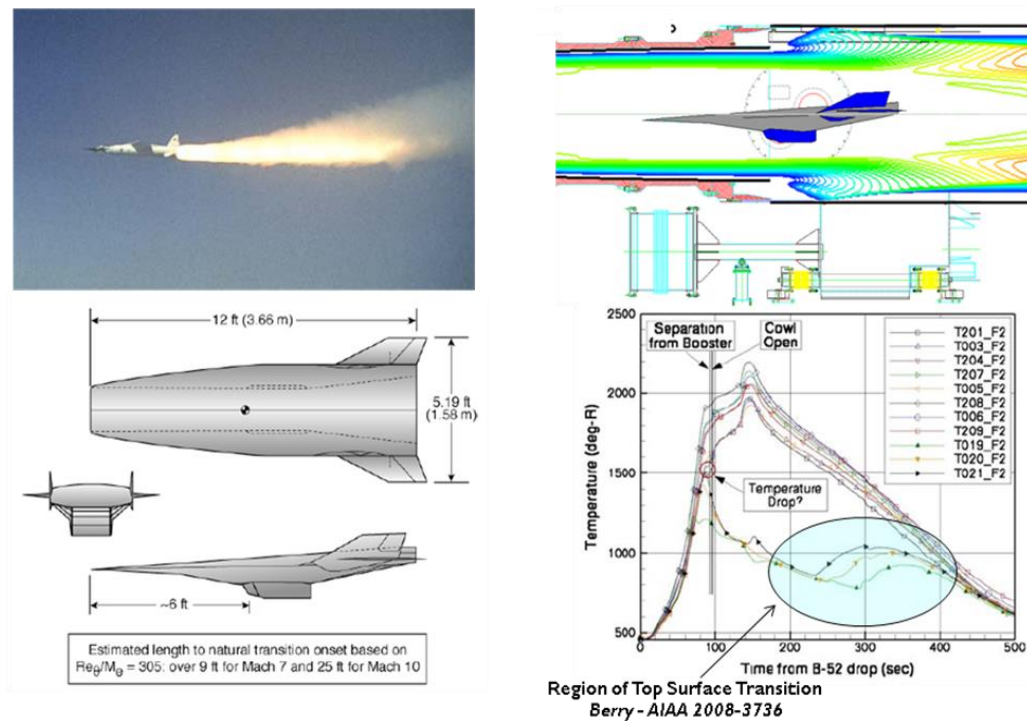
Figure 38: Ground Test and Computational Comparison to Existing X-43 Boundary Layer Transition Flight Data
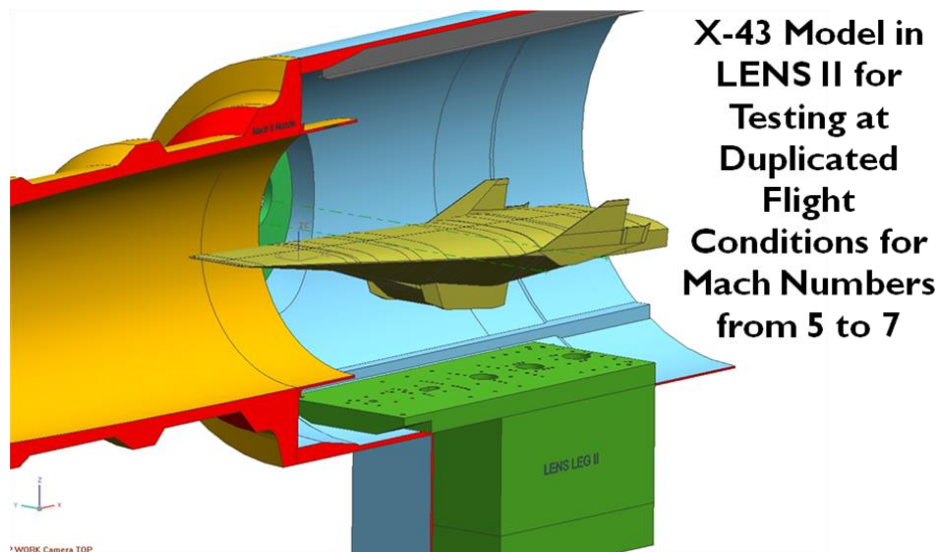

Figure 39: Full-scale X-43 Model for Flight Matching Boundary Layer Transition Studies
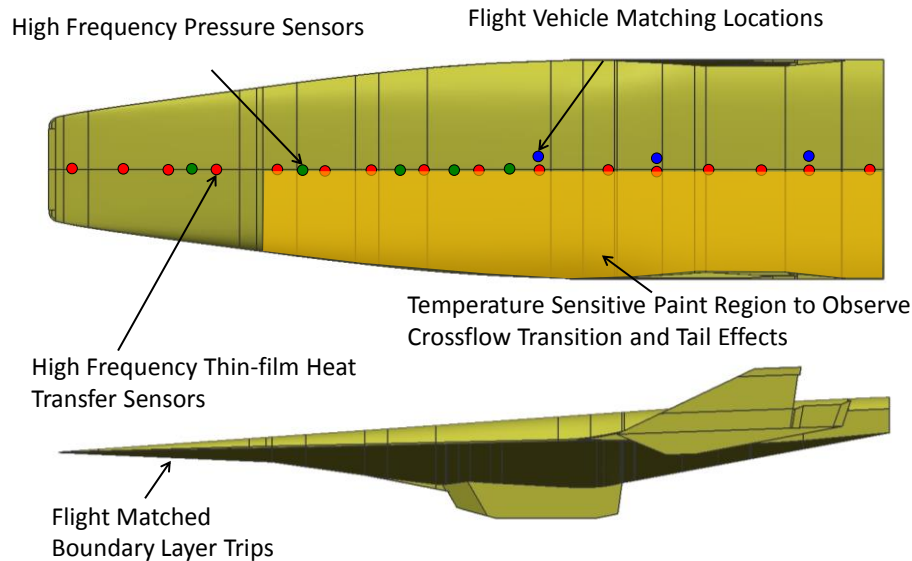
Figure 40: Features of Full-scale X-43 Model for Boundary Layer Transition Studies

Within the past 10 years, we have conducted a large number of studies for NASA associated with the aerothermal loads on the X-38, space shuttle, and CEV capsules; Figure 41 shows a number of models which have been tested in the LENS 1 facility in these programs. In support of NASA's shuttle program, extensive studies were conducted to evaluate the heating loads on the leading edge and windward surfaces resulting from surface discontinuities such as protuberances and cavities. Here rectangular trips and cavities were located in key areas (see Figure 42) and detailed heat transfer measurements were made with thin-film gages and temperature-sensitive paint to evaluate the downstream effects of tripping with particular emphasis on leading edge heating rates which are increased significantly when transition occurs on the attachment line.

Figure 41: Boundary Layer Transition Studies for NASA Ascent and Re-entry Vehicles
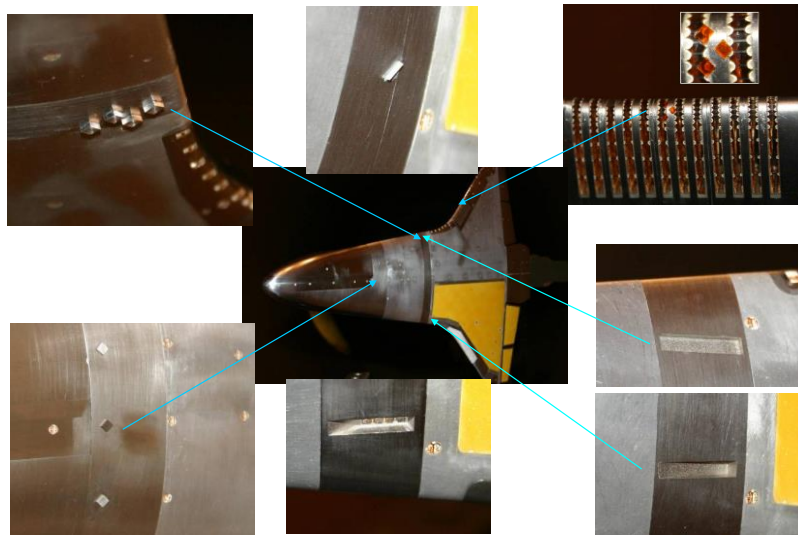
Figure 42: Boundary Layer Transition Objectives – Protuberances and Cavities

As in our earlier studies on cones, the thin-film gages gave us detailed information on the transition characteristics (see Figure 43); in particular the first indications of transition via the occurrence of turbulent bursts and definitive information on the intermittency through the transition region. Transitional and turbulent flows can, of course, create a significant increase in the heating loads to the flap control systems as illustrated Figure 44.
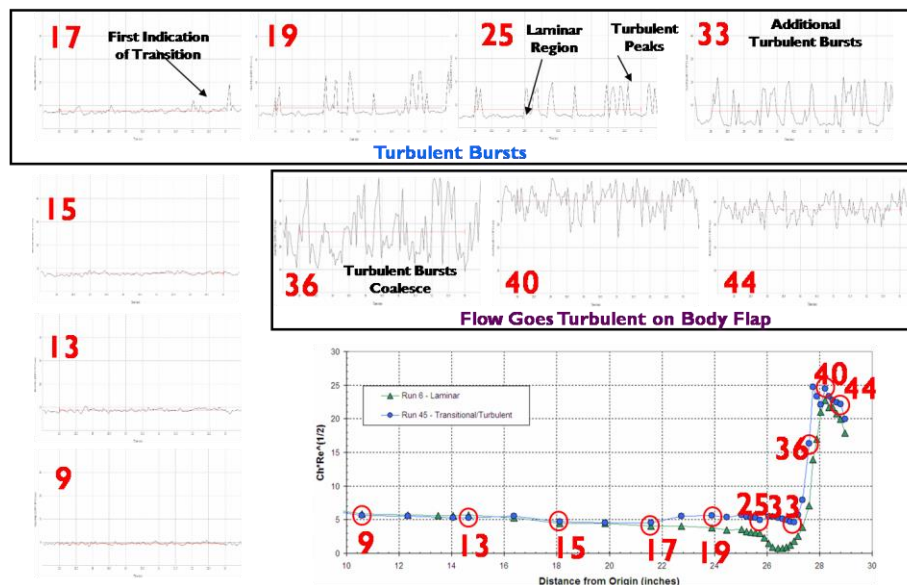

Figure 43: Expanded Transition Region Plot with Thin-film Time History Traces (millisecond time rate)
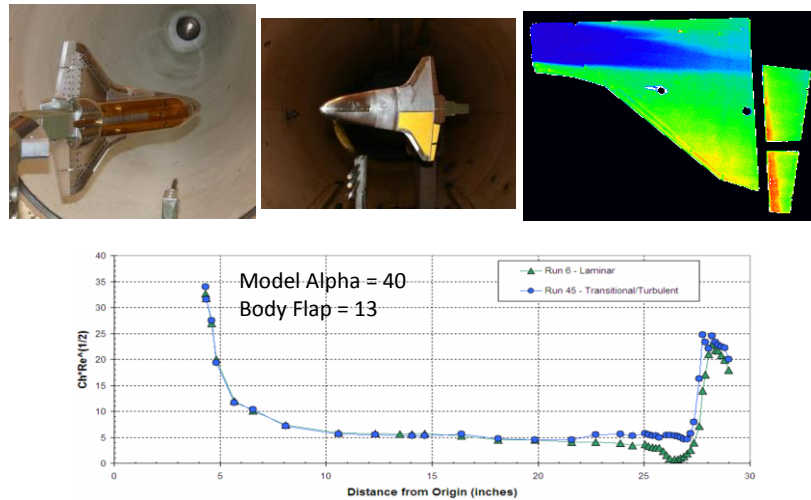
Figure 44: MH-13 Space Shuttle Orbiter Re-entry Boundary Layer Transition Experiment

The occurrence of boundary layer transition on the heat shield of the re-entry capsule is of major concern to the designers of the heat shield because it increases the heating load by factors from 2 to 3 as illustrated in Figure 45. Of major concern are the heating loads on the windward shoulder of the vehicle where a combination of turbulent heating and surface roughness effects can result in major augmentation in the heating rates relative to the laminar values.
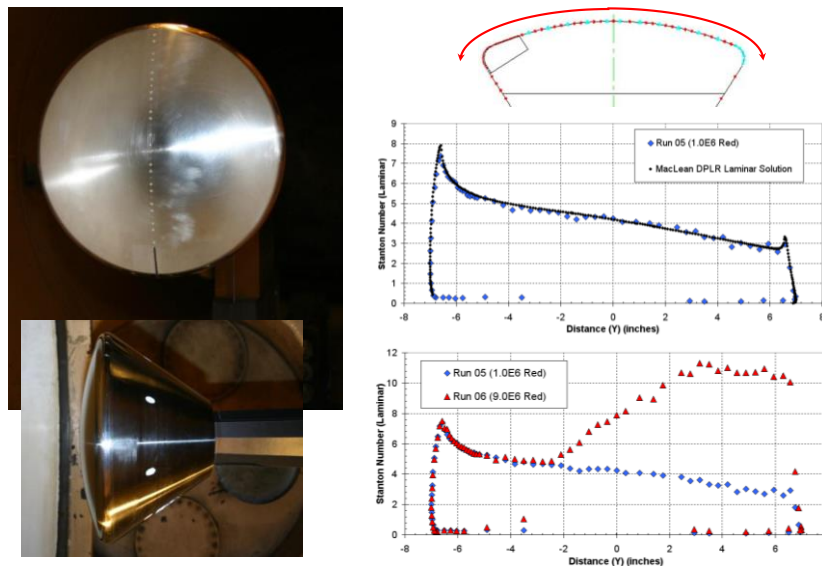

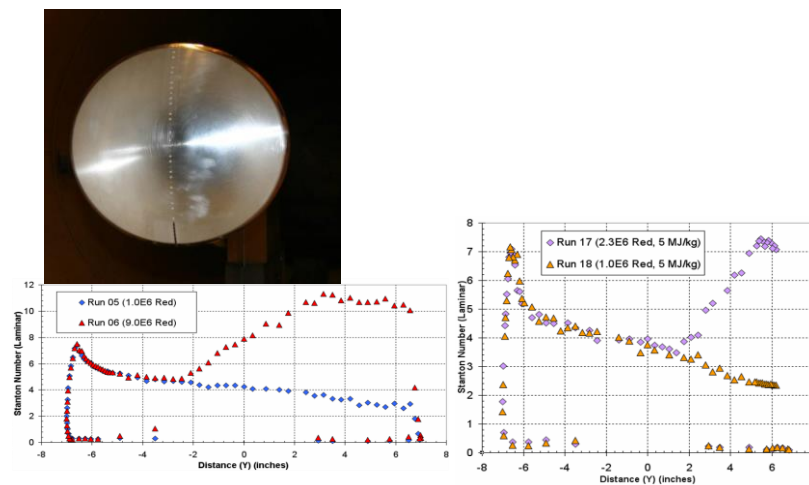**Figure 45: 7.0% Scale CEV Model Installed in LENS I**

Figure 46: Real Gas Effects on Boundary Layer Transition and Turbulent Flows

In these studies we also investigated how transition on the capsule face was influenced by real gas effects and Figure 46 indicates that transition is delayed under higher enthalpy conditions. To further investigate these effects under flight conditions, we are preparing ground tests to be conducted for direct comparison with flight data obtained in the re-entry program. These tests which will be conducted in the LENS XX facility would duplicate the velocity/altitude conditions obtained in flight with a full-scale replica of the re-entry blunted cone (see Figures 47 and 48).
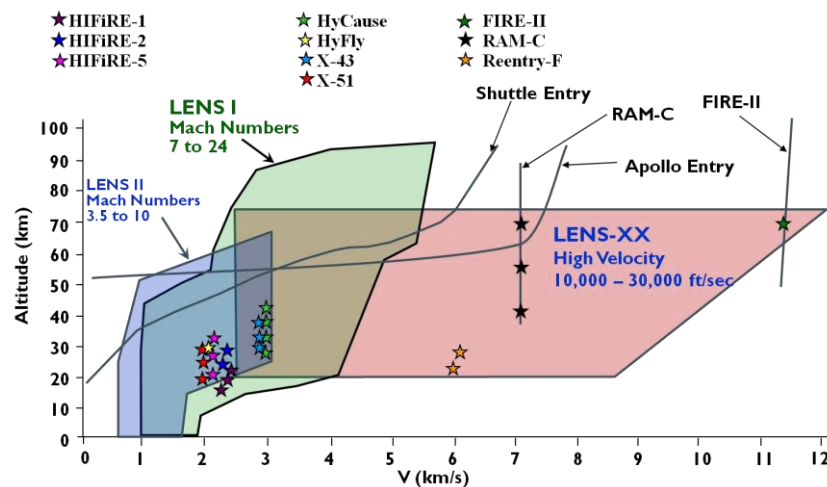

Figure 47: Velocity/Altitude Conditions for Full-scale Duplicated Ground-to-Flight Comparisons in LENS Facilities
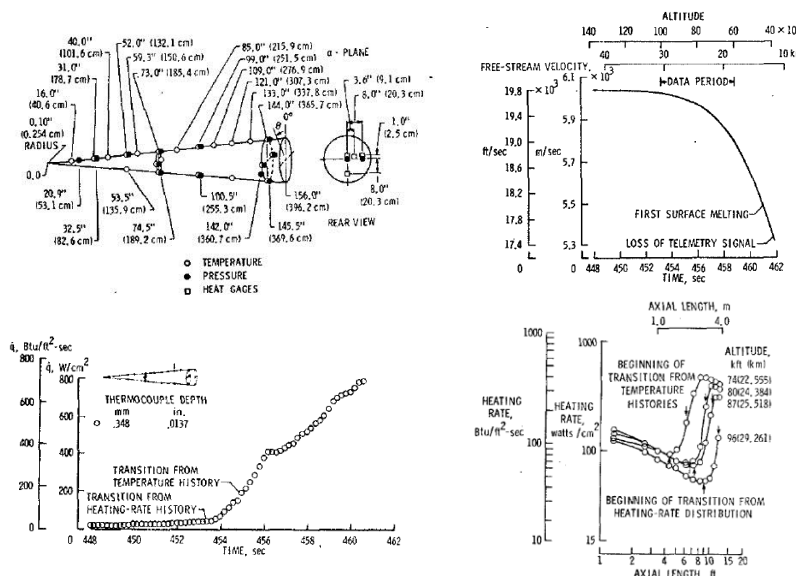
Figure 48: Proposed Tests in LENS XX of Full-scale Re-entry-F Configuration for Direct Comparison to Flight

4.0 LAMINAR AND TURBULENT SHOCK INTERACTION STUDIES

4.1 Comparisons between Prediction and Experiment for Regions of Shock Wave/Laminar Boundary Layer Interaction in Hypersonic Flows

Experimental studies to evaluate the characteristics of regions of laminar and turbulent shock wave/boundary layer interaction have been pursued by researchers at CUBRC for the past 45 years with the objective of developing accurate methods to predict the size of large aerothermal loads developed in these flows. While early work revolved around solving the boundary layer equations, this approach was quickly replaced when computers were developed of a size and speed to enable direct solutions to the Navier-Stokes solutions to be obtained. While a number of Navier-Stokes computations have been successfully employed to describe regions of laminar shock wave/boundary layer interaction, the first definitive sets of solutions which were in good agreement with measurements obtained in the CUBRC tunnels were obtained by Hung and MacCormack as illustrated in Figure 49. Further computations by Rudy accounted for three-dimensional effects associated with the finite span of the "two-dimensional" models employed in the experiments. However, subsequent code validation activities pursued by ESA and by Candler raise serious questions on the accuracy of the numerical schemes and the gridding employed to obtain accurate solutions for these flows. These issues were addressed in obtaining solutions to code validation experiments by Holden using hollow cylinder/flare and double cone configurations. Experimentally, issues associated with vibrational nonequilibrium and real gas effects were addressed and measurements were conducted at low Reynolds numbers to allow further computations to be made using the DSMC technique. Although for laminar flows most issues associated with the numerical schemes, gridding and "artificial viscosity" have been resolved, describing the flow chemistry in high-enthalpy flows such as those developed over the flap of the shuttle have not been solved, and experiments are continuing to provide definitive measurements in

fully laminar flow to evaluate and improve the models of flow chemistry used to describe high-temperature separated flows induced by shock wave/boundary layer interaction (see Figure 50).
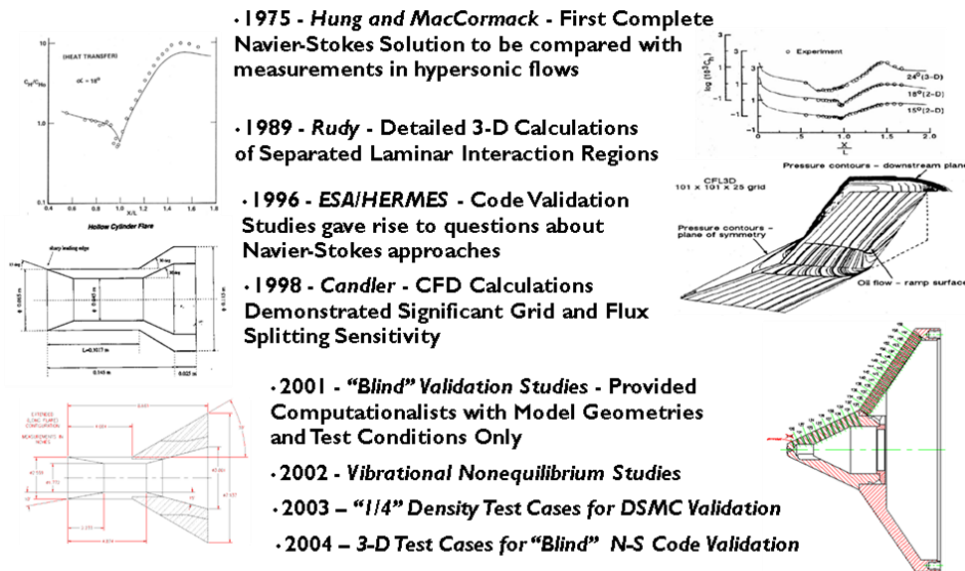

Figure 49: History of Comparisons of CUBRC Measurements and Predictions for Hypersonic Laminar Flows
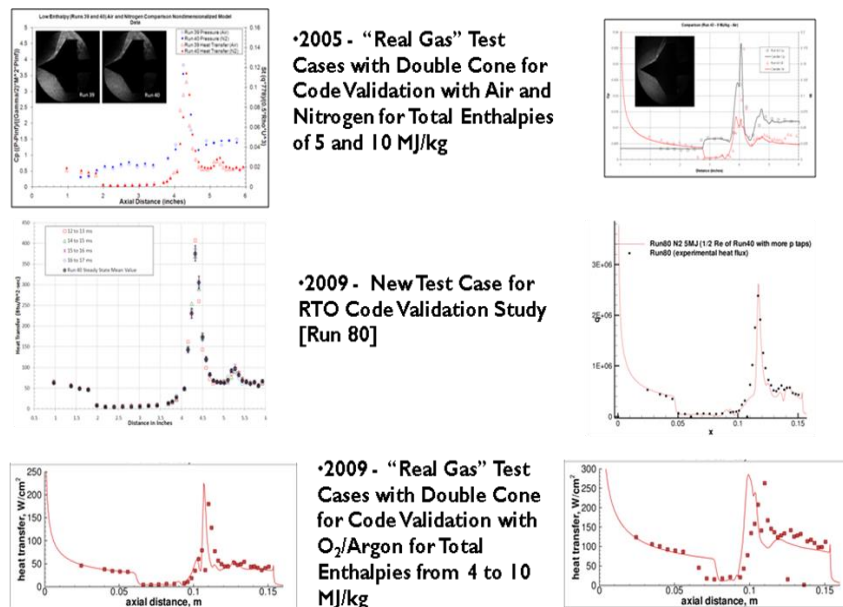

Figure 50: History of Comparisons of CUBRC Measurements and Predictions for Hypersonic Laminar Flows (cont)
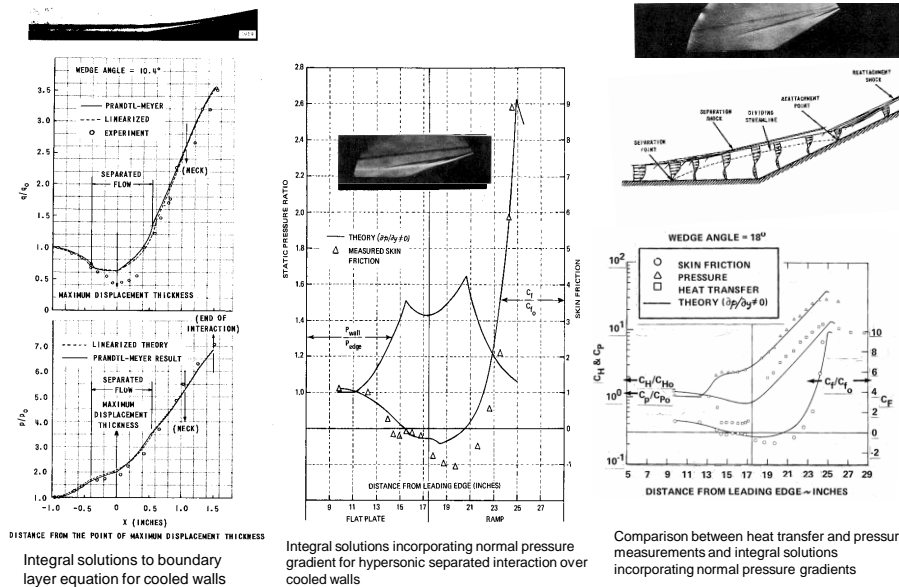
Figure 51: Integral Methods to Describe Pressure and Heat Transfer Distributions in Laminar Separated Regions induced by Shock Wave/Boundary Layer Interactions (Holden 1966)

Examples of predictions made with solutions for the boundary layer equations are shown in Figure 51. While in supersonic flows this approach can yield good results, in hypersonic flows, where the normal pressure gradients in the separation and reattachment regions are large, only by solving the second order boundary layer equations incorporating normal pressure gradients is it possible to obtain reasonable solutions. However, for laminar separated flows, the only rational approach is to use Navier-Stokes or DSMC methods, and with these techniques it is possible to obtain excellent agreement with experimental data as shown in Figure 52.
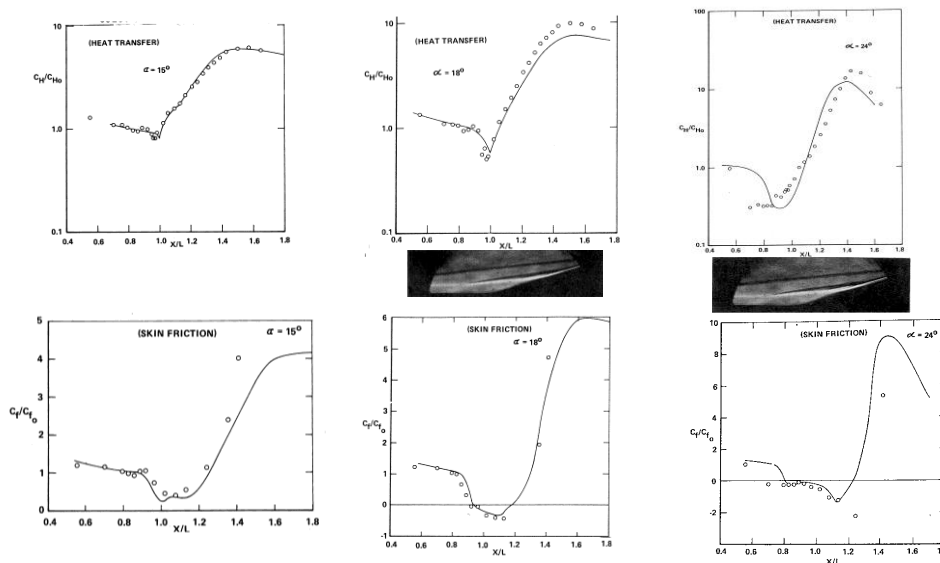

Figure 52: Comparisons with Measurements of Heat Transfer and Skin Friction Distributions and NS Solutions for Attached Incipient-separated and Well-separated Flows (Hung and MacCormack 1975)
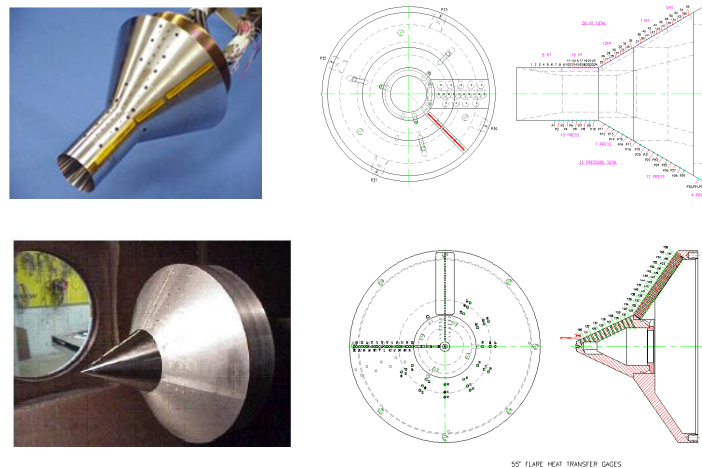
Figure 53: Hollow Cylinder/Flare and Double Cone Configurations for 2001 "Blind" Validation Studies

Further examples showing comparisons between measurements and predictions for flows over the double cone and hollow cylinder/flare configurations (Figure 53) are shown in Figures 54 and 55. The initial comparisons were made in the "blind validation" study conducted in 2001 and were updated a year later to include the effects of vibrational nonequilibrium. In the nitrogen freestream, both Candler and Gnoffo's results show an overprediction in the heat transfer rate which was later demonstrated to result from slip effects over the forecone. Initially, the DSMC methods did not produce results of comparable accuracy; however, as a result of these studies, new models were incorporated into this code to improve their accuracy at the higher Reynolds numbers. At the same time, slip effects were incorporated into the Navier-Stokes solution and the comparisons shown in Figures 56 and 57 show excellent agreement between both techniques and the experimental data. Measurements were made with the double cone and hollow cylinder/flare configurations to examine abilities of the Navier-Stokes computation to predict three-dimensional separated flows. Computations of the flow over the double cone at 2° angle of attack were performed by both Nompelis and Miller with mixed results. As shown in Figure 58, Nompelis predicted the distribution of heat transfer and pressure on the leeward ray with reasonable accuracy but significantly underpredicted the size of the separated region on the windward ray where as Miller's calculations produced the opposite results. Despite the fact that the measurements on the hollow cylinder/flare configuration (see Figure 59) provided an excellent test case, no one has yet performed calculations to compare with these measurements.
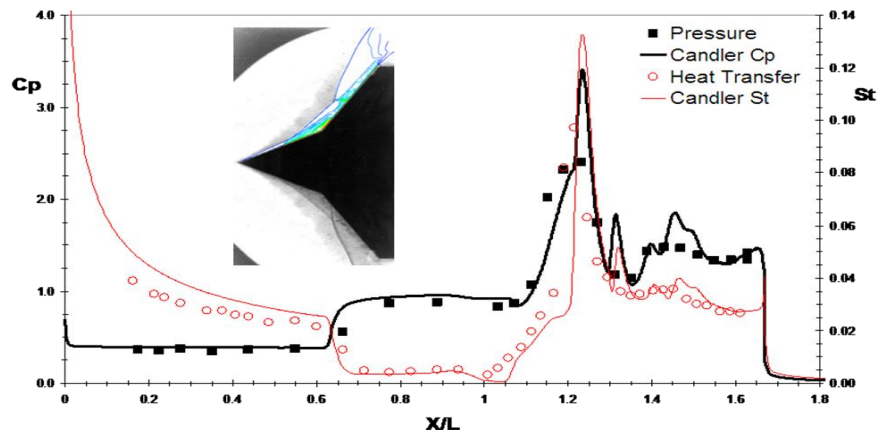
Figure 54: Example of Comparisons between Heat Transfer and Pressure Measurements on 25°/55° Double Cone Configuration in a "Blind" Validation Study
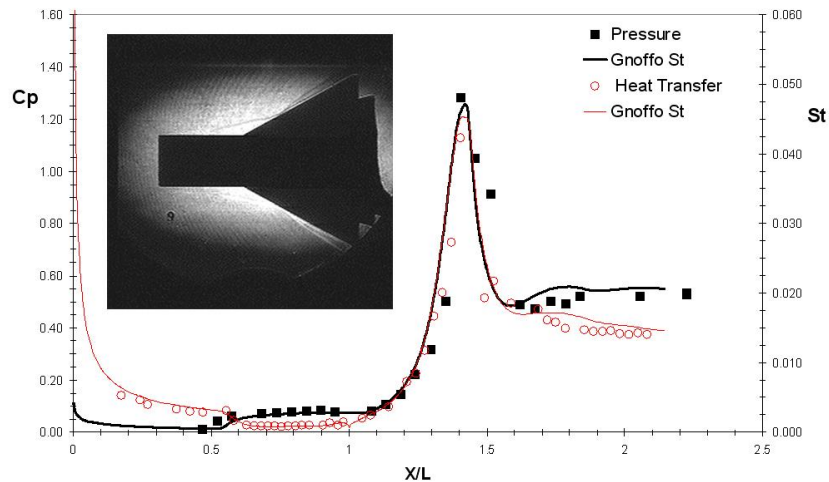
Figure 55: Example of Comparisons between Heat Transfer and Pressure Measurements on Hollow Cylinder/Flare Configuration in Low Reynolds Number Flow and Gnoffo's Computation including Vibrational Nonequilibrium Effects
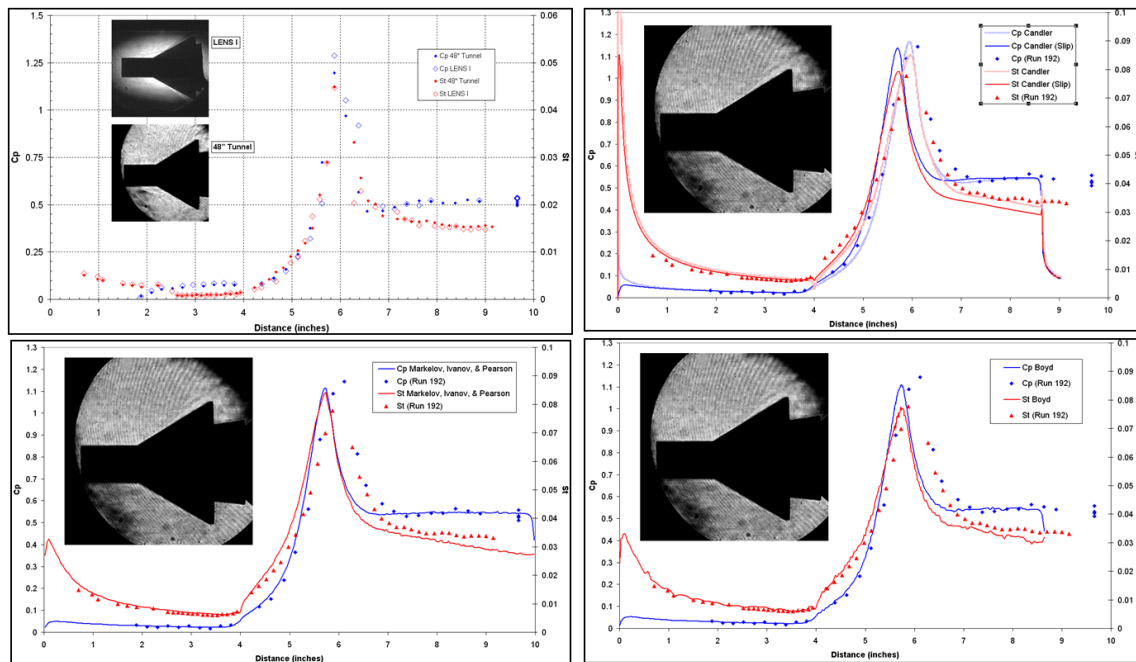
Figure 56: Comparisons with Additional Measurements on Hollow Cylinder/Flare Configuration in Hypervelocity Nitrogen Flows and Improved Navier-Stokes and DSMC Code Predictions
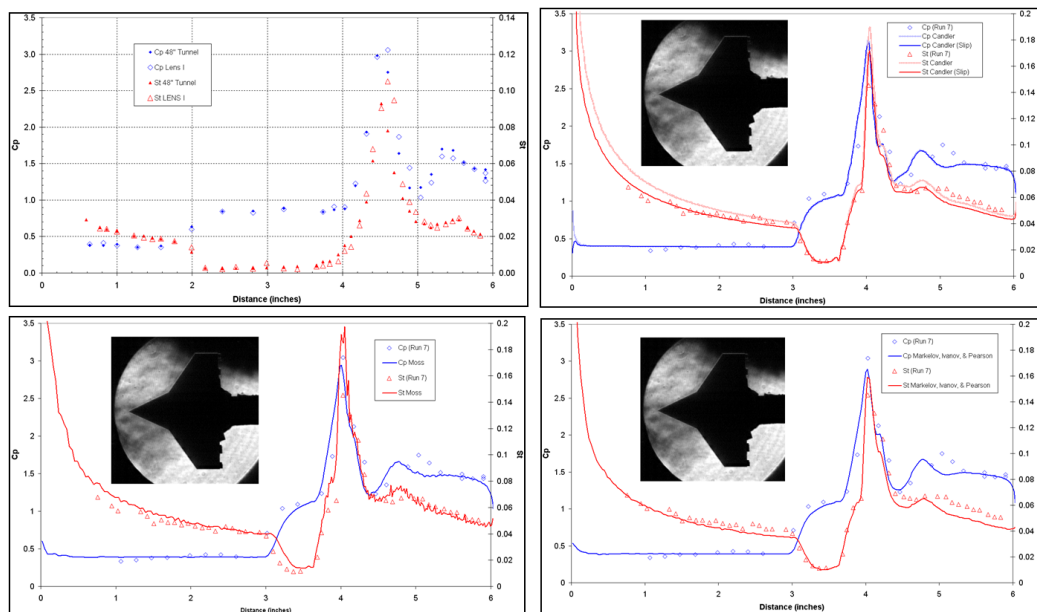
Figure 57: Measurements on Double Cone Configuration and Comparisons with Improved Navier-Stokes and DSMC Predictions
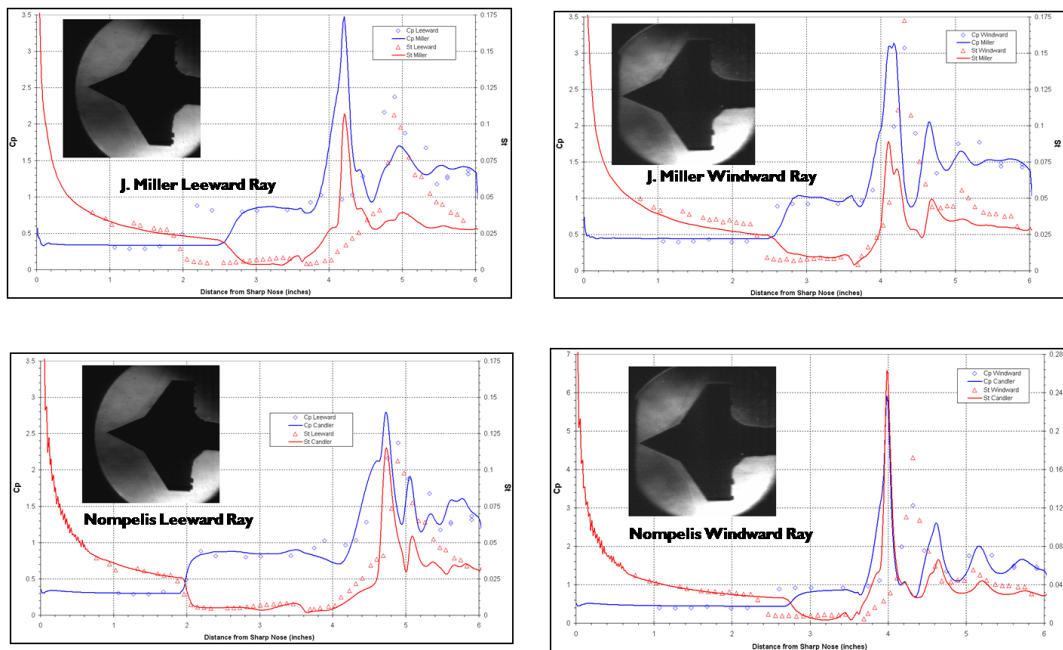
Figure 58: Comparison between Numerical Predictions and Double Cone Measurements for 2° Angle of Attack
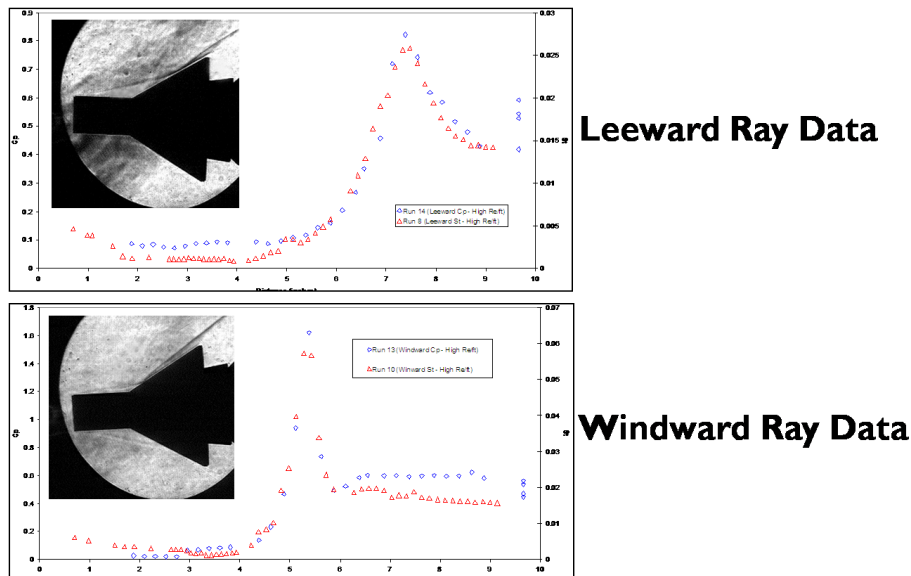
Figure 59: Heat Transfer and Pressure over Hollow Cylinder/Flare Configuration at 2.5° Angle of Attack (no CFD results)

Later in comparisons conducted in the RTO studies of computation methods to describe laminar hypersonic flows, comparisons were made with a relatively high Reynolds number nitrogen flow over a double cone configuration (Run 40). Previously calculations had been accomplished for a run in air at

similar test conditions, which were in excellent agreement with the measurements. However, in the nitrogen flow, many of the computations showed that a steady separated region was not attained in times comparable with the test times for the experiments. An examination of the test data at this condition shown in Figure 60 demonstrated that the flow reached a steady condition within 2 ms and remained stable in size for an additional 6 ms. The discrepancy between this set of measurements and this set of test data has yet to be resolved. However, to ensure that this problem was not related to potential instability effects in the reattachment region, we ran experiments (Run 80) at half the Reynolds number of the earlier test case. Additional instrumentation was also added to more accurately define the distribution of pressure and heating in the separation and reattachment regions. This case did not result in the computational problems observed earlier, and Nompelis' "blind" computations are shown to be in excellent agreement with the experimental data.
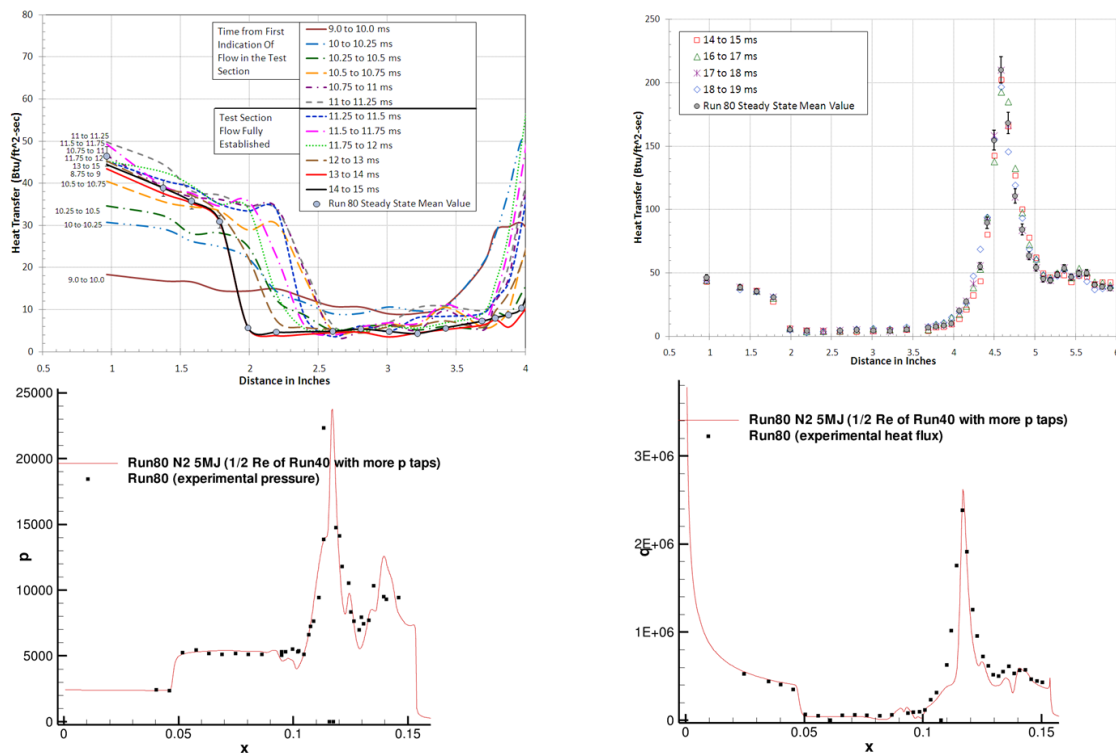
Figure 60: Comparison of Experiment and Converged CFD Calculations for Run 80 (1/2-RE of old Run 40)

In the earlier studies over the double cone configuration, it was demonstrated that although measurements in air and nitrogen at total enthalpies of 5 MJ/kg were in excellent agreement with experiment, calculations by both Candler and Gnoffo significantly underpredicted size of the separated region and more importantly the structure and heating rate in the reattachment/compression region on the second cone as shown in Figure 61.
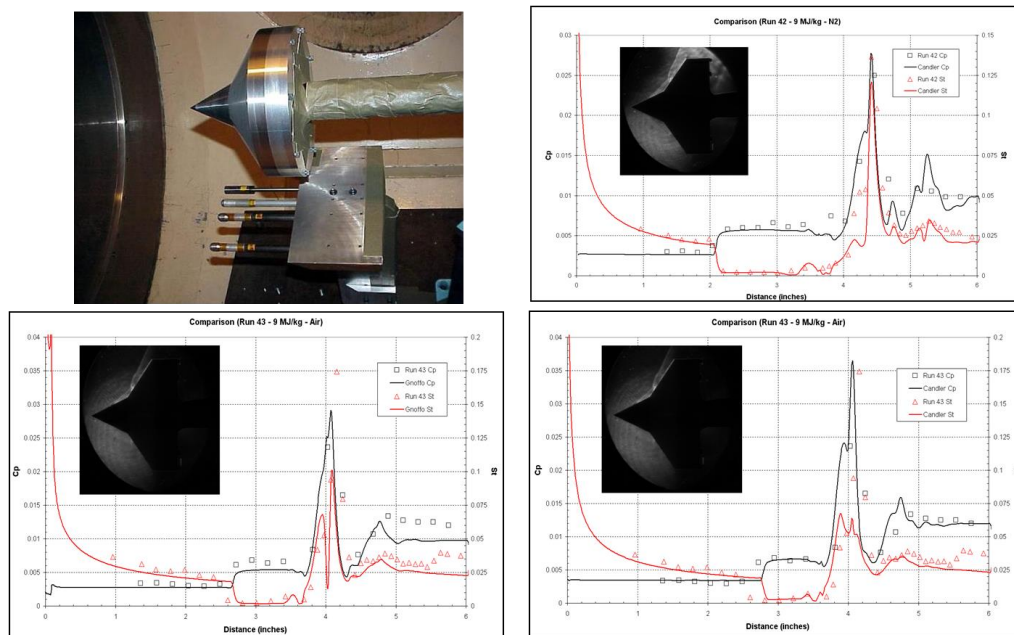
Figure 61: Measurements on Double Cone Configuration Showing No Real Gas Effects in Air and Nitrogen at 5 MJ/kg but Significant Effects in Air at 9 MJ/kg

Recently, in studies to attempt to resolve the cause of this phenomena, measurements were made with a double cone configuration for a range of total enthalpies with mixtures of oxygen and argon as a freestream gas (see Figure 62). While the computations in pure oxygen at 4 MJ/kg are in excellent agreement with experiment (Figure 63), the computations in the same gas at 10 MJ/kg again show that the size of the separated region is significantly underpredicted (Figure 63). Discrepancies between measurements and computations in the attached flow over the forecone (see Figure 64) indicates that the problem may lie in the modeling of flow chemistry in the nozzle with the resultant inaccuracies in the freestream conditions. To eliminate these problems we plan additional studies in the LENS XX expansion tunnel running at conditions where temperatures in the test gas will stay below those where flow chemistry in the freestream becomes an issue.

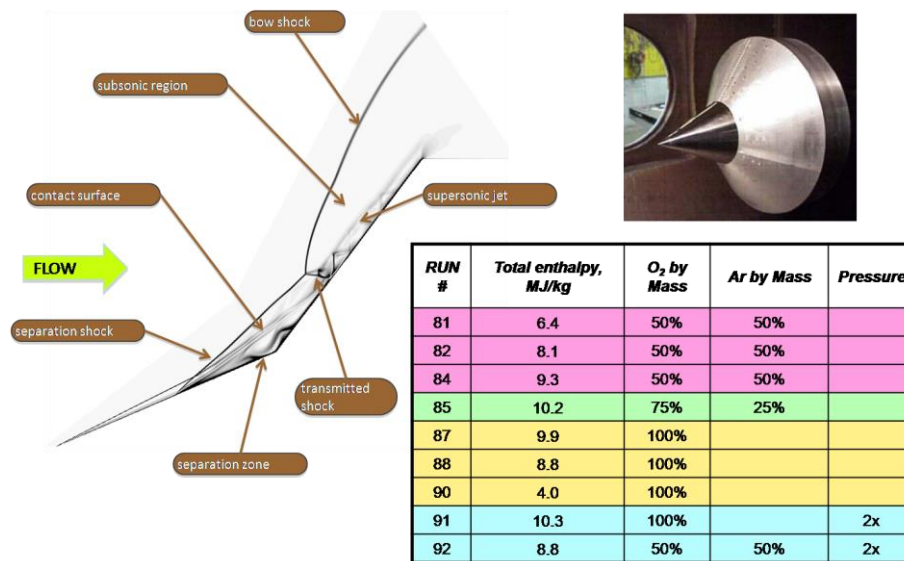| RUN #	Total enthalpy, MJ/kg	O₂ by Mass	Ar by Mass	Pressure
81	6.4	50%	50%	
82	8.1	50%	50%	
84	9.3	50%	50%	
85	10.2	75%	25%	
87	9.9	100%		
88	8.8	100%		
90	4.0	100%		
91	10.3	100%		2x
92	8.8	50%	50%	2x

Figure 62: Continuing Studies of Real Gas Effects on Double Cone Flowfield in Oxygen/Argon Freestream Flows
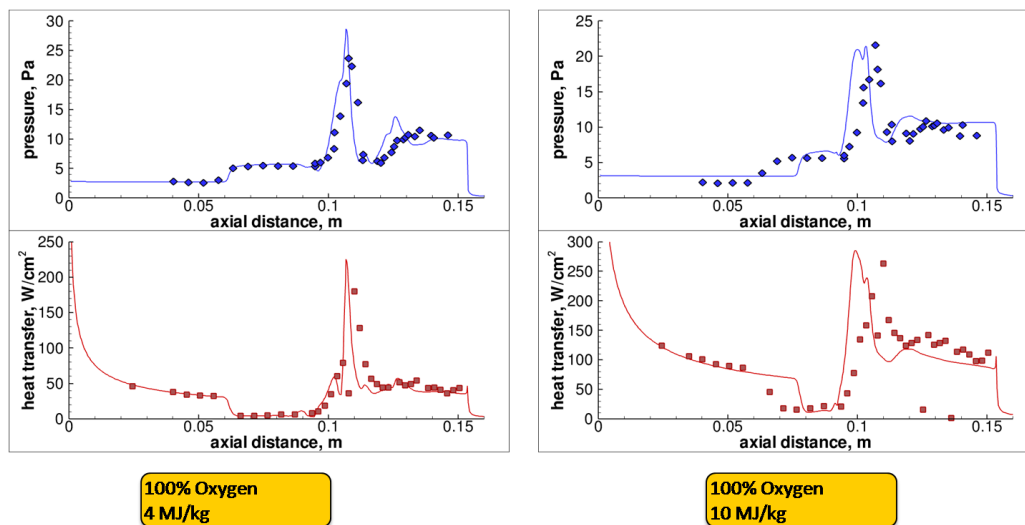

Figure 63: Comparisons between Pressure and Heat Transfer Measurements and Prediction for Double Cone in Low- and High-enthalpy Oxygen Flows
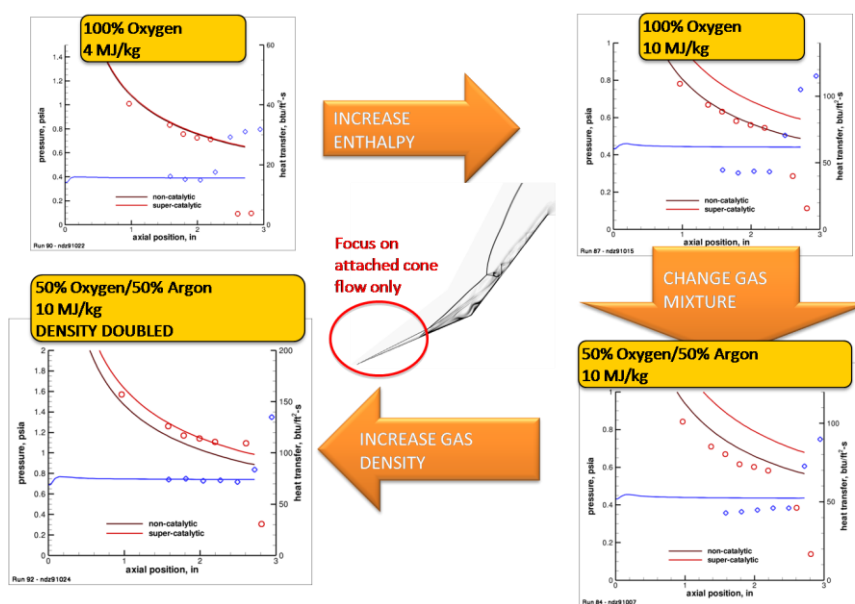
Figure 64: Comparisons of Attached Forebody Cone Data to CFD for Four Cases from Oxygen/Argon Study

4.2 Comparisons between Prediction and Experiment for Regions of Shock Wave/Turbulent Boundary Layer Interaction in Hypersonic Flows

While, as discussed above, with the exception of real gas effects, the size and properties of laminar interaction regions in supersonic and hypersonic flows can be predicted with accuracy, the same cannot be said for predicting turbulent separated regions. In fact, with the exception of some computations tuned to a specific experimental condition, there are no prediction methods with well-established turbulence models that are capable of predicting the size and properties of separated regions induced by incident shocks and compression corners as well as those behind steps and in cavities. The aerothermal loads developed in regions of shock wave/boundary layer interaction in supersonic and hypersonic flows provide the most stringent requirements for the design of thermal protection systems as was the case for space shuttle design (see Figure 65) and control systems for maneuverable interceptors and re-entry vehicles. Also the detailed flow and combustion processes in scramjet propulsion systems are highly dependent on the structure and characteristics of regions of shock wave/turbulent boundary layer interaction as illustrated in Figure 65. The mechanism of flow separation in regions of shock wave/turbulent boundary layer interaction is significantly different from those in laminar flows. As illustrated in Figure 66, for both wedge- and externally-generated regions of shock wave/boundary layer interaction, flow separation in turbulent flows first occurs in the sublayer at the base of the turbulent boundary layer and the separation shock is propagated through the unsteady structure of the turbulent boundary layer before it reaches the freestream. This is also the case for the shocks generated in the reattachment region. The interaction between the turbulence in the boundary layer and the shock propagated through it significantly complicates the modeling of turbulence to describe these flows.
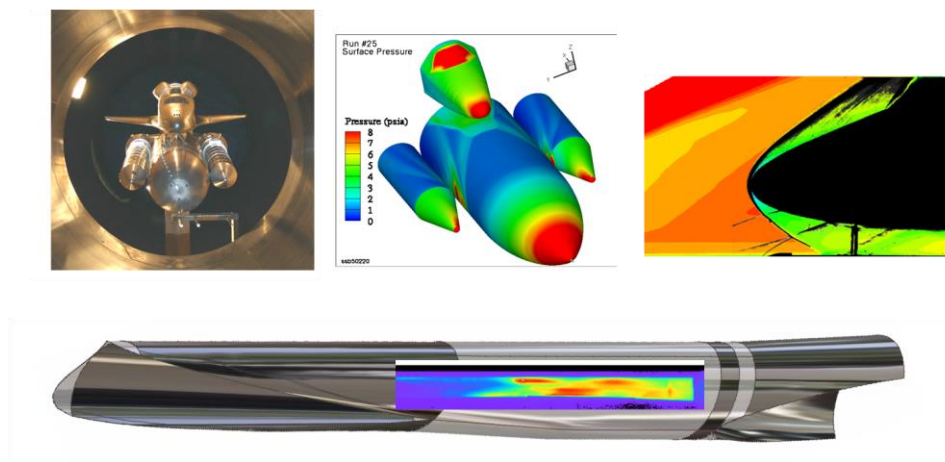
Figure 65: Shock Wave/Turbulent Boundary Layer Interaction Phenomena
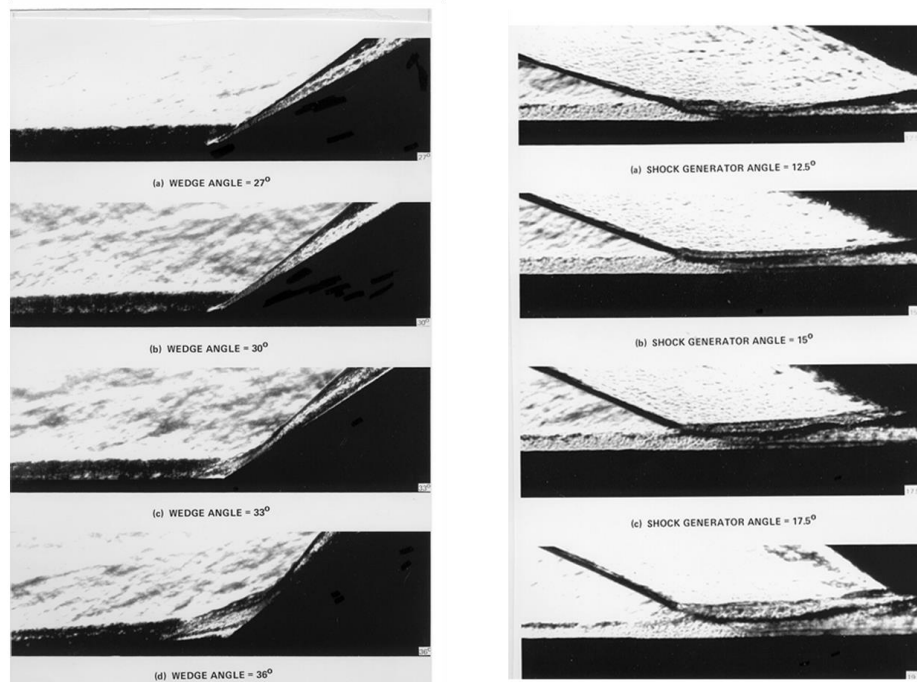
Figure 66: Wedge- and Externally-Generated Shock-Induced Turbulent Separated Flows at Mach 8

Currently we are pursuing an experimental program to provide measurements with which to construct and evaluate models of turbulence which can be used in the Navier-Stokes and LES prediction methods for high Reynolds number supersonic and hypersonic flows. This program involves conducting experiments in support of the design of flight programs as well as fundamental studies in high Reynolds number flows over large generic models to obtain detailed flowfield measurements to directly evaluate the accuracy of turbulence models. We have been directly involved in the design of the cone/cylinder/flare and elliptic cone configurations to be tested in the HIFiRE program (Figure 67). Here of specific interest to the modeling of shock wave/turbulent boundary layer interaction, we have

obtained measurements to examine the separated flow over the cone/flare junction of the HIFiRE 1 configuration and compared our measurements with the predictions based on Navier-Stokes codes. The model and instrumentation used in studies with a full-scale replica of the HIFiRE 1 configuration are shown in Figure 68. The experimental program was conducted at duplicated flight conditions for a range of trajectory points to obtain fully developed turbulent flows ahead of the flare. We tested a number of flare configurations and as shown in Figure 68, we extended the length of the flare to obtain data for a configuration where the downstream conditions could be accurately specified. Initially a 37° flare angle was proposed for the flight configuration based on Navier-Stokes calculations. However, as shown in Figure 69, the size of the separated region observed in our experiments was significantly larger than that predicted and our experiments indicated that reattachment occurred on the trailing edge of the flap making this configuration unsuitable for comparison with computation. Further experiments showed that a flare angle of 30° would be too small to produce significant separation, and finally, a configuration with a 33° flare would give a separated region of sufficient size to provide well defined experimental measurements of the separation and reattachment process.
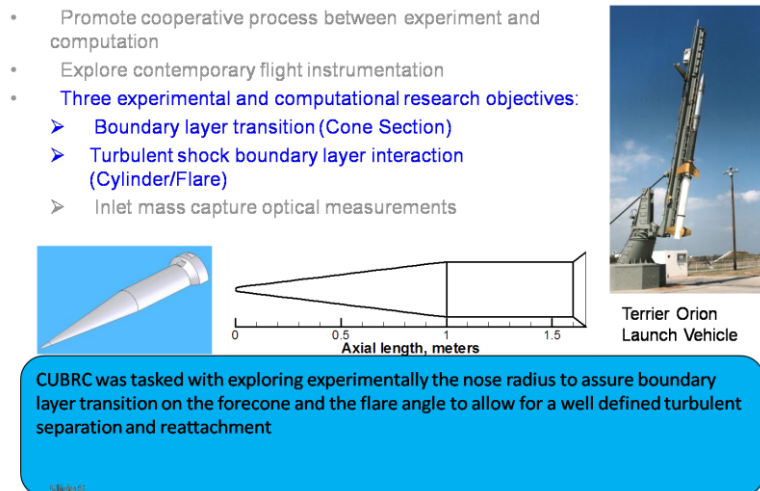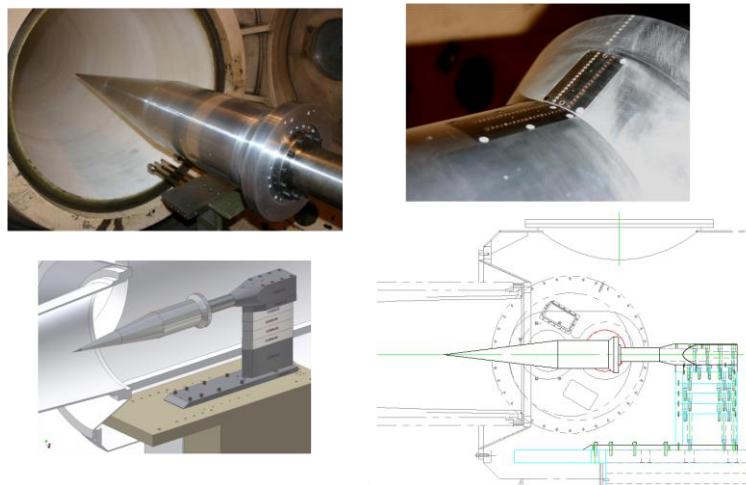

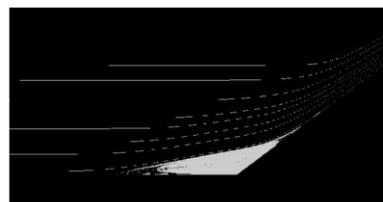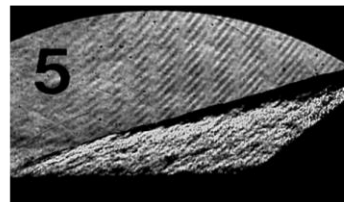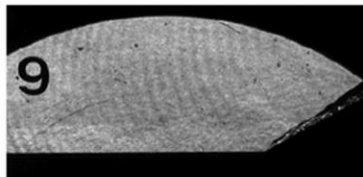**Figure 67: HIFiRE Program Objectives and Experimental Background**

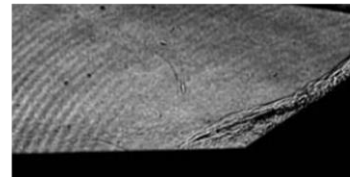**Figure 68: HIFiRE 1 Model Installed in LENS 1**

Preliminary Computations Study with 37° Flare

Experimental Study with 37° Flare Shows Considerably Larger Region

CUBRC Modified 30° Flare Shows Only Small Evidence of Separation

Further Modification to 33° Flare Angle Shown Good Separation and Reattachment

Figure 69: Comparison of Experiment and AVUS Solution on HIFiRE 1 Flare

However, as mentioned earlier even this configuration represented compromise because as shown in Figure 70, only by extending the flare could we obtain a well-defined constant pressure region downstream of the reattachment point, which would provide more accurate downstream conditions for prediction. As shown in Figure 71, there were other features of this flow of concern, and in particular, the establishment of fully turbulent flow over the cone and the potential occurrence of relaminarization at the cone/cylinder junction. To obtain a satisfactory resolution of these conditions, a number of runs were undertaken resulting in selection of the geometry of the blunt nosetip and the test conditions at which the flow remained fully turbulent approaching the flare. For the conditions selected we performed computations employing a number of different models for turbulence in DPLR solutions to the Navier-Stokes equations. The results of these predictions varied from a fully attached flow for the Spalart-Allmaras (SA) turbulence model to a significantly larger separated region for the shear stress transport model (SST) as shown in Figure 72.
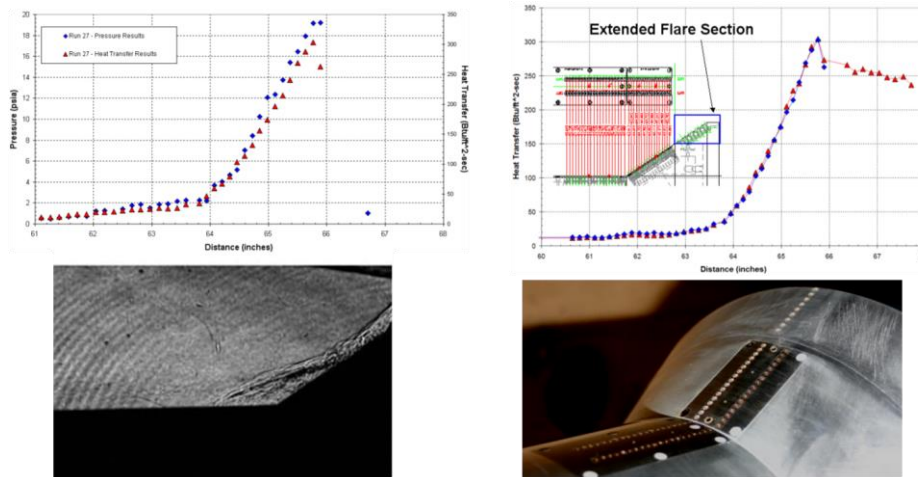
To achieve a well defined experiment for code validation CUBRC extended the flare section. Flight vehicle configuration does not allow for extension.

Figure 70: Measurement of Flare Results in Second Entry and Extension of Flare

- The complete test matrix includes angle of attack, tripping, and other permutations.
- Here, we consider only axisymmetric, natural transition cases.

flare interaction field

expansion (relaminarization?)

turbulent cone heating

forebody transition
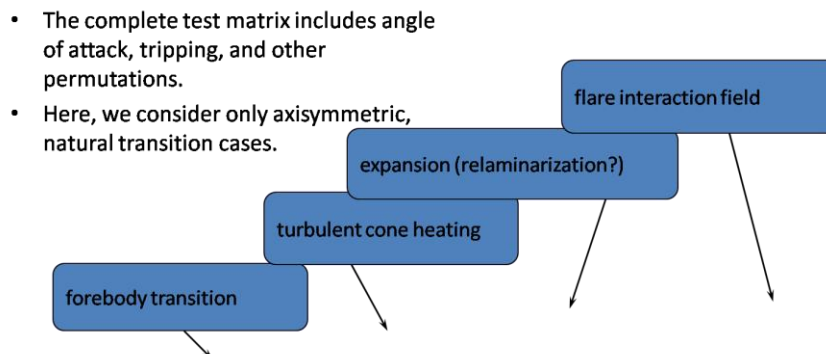
Figure 71: Computational Analysis of HIFiRE 1 Interaction Region

M=7.16, r=2.5-mm

EXPERIMENT (Run 14)

Shear Stress Transport (SST) Model

Spalart-Allmaras Model

- Full vehicle computed with SA and SST models 33° flare shown.
- For Phase-I Schlieren data only was available to compare with
- SA predicts no separation, SST predicts over 2X the measured separation.
- SST2003 uses a Sarkar-type mixing-layer correction term that causes even larger separated regions than without.
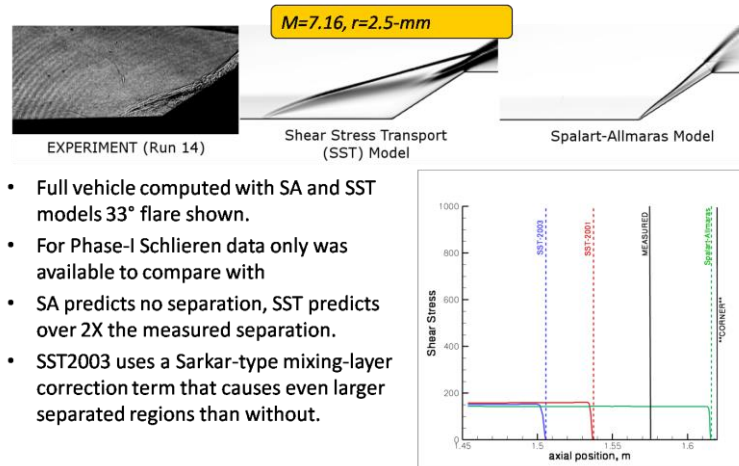
Figure 72: Flare Heating with RANS Models – Phase 1

Further studies to find more satisfactory models of turbulence to describe these flows resulted in employing a "stress limiter" to control the rise of Reynolds stress caused by the rapid production of kinetic energy in the separated region. Here we used the SST model combined with Wilcox Stress Limiter (see Figure 73) and employing a "stress limiter" factor of 0.9, we were able to match the size of the separated region (see Figure 74) and more accurately predict the pressure and heat transfer distribution throughout the interaction region (Figures 75 and 76).

- Wilcox stress limiter limits rise in Reynolds stress (eddy viscosity) caused by rapid production increase of turbulent kinetic energy.
- SST model has something like this already built-in and acts too aggressively to restrict Reynolds stress (implicitly C_{LIM}=1.0).
- We can easily adjust this by selecting a lower coefficient value. I liked 0.90 for this case (Wilcox recommends 0.875 for his model, which is close).
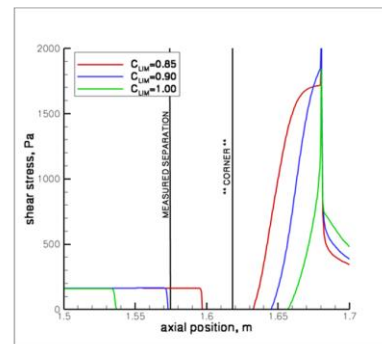
$$\mu_T = \frac{\rho k}{\max\{\omega, (1.0)\Omega F_2 / \sqrt{\beta^*}\}}$$

C_{LIM}

Figure 73: Flare Heating Prediction with Modified Reynolds Stress Limiter
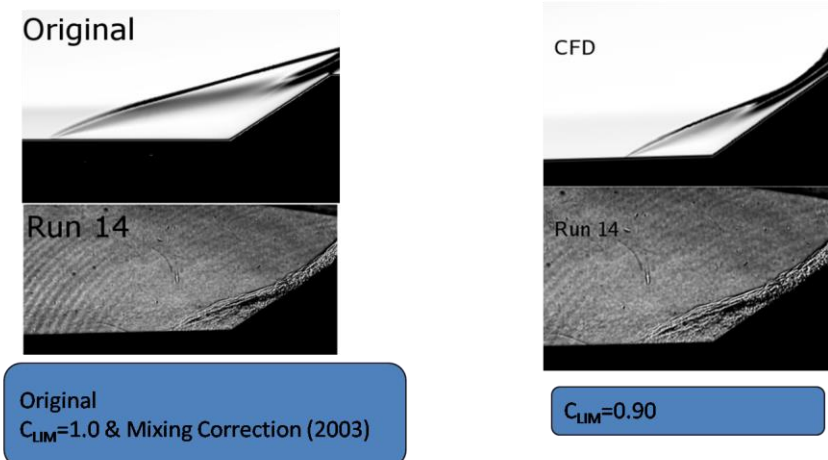
- Adjusting stress limiter coefficient on SST model provides accurate qualitative agreement.

Figure 74: Flare Heating Prediction with Modified Reynolds Stress Limiter, C_{LIM} = 0.90

- Flight configuration flare reattaches, but does not extend far enough downstream to asymptote to a constant pressure
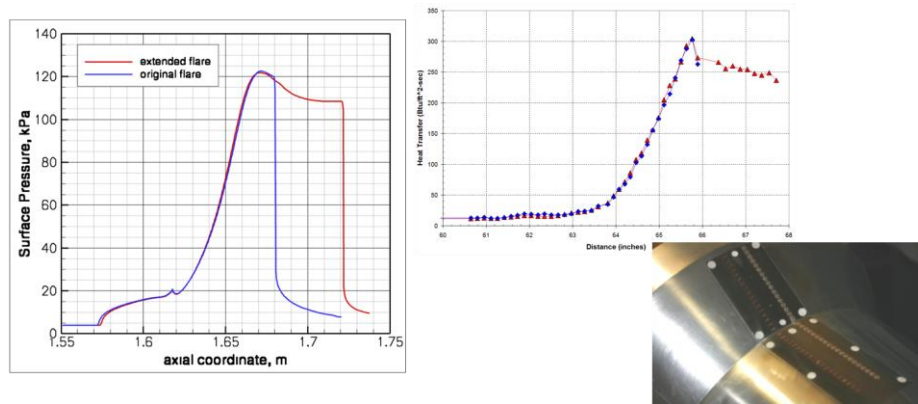- An extended flare was used in the ground test for many runs to get better code validation data.
- Experiments were performed to compare the long & short flares and the data is identical at the same axial positions.

Figure 75: Design of Phase II Instrumented Flare with Improved Modeling
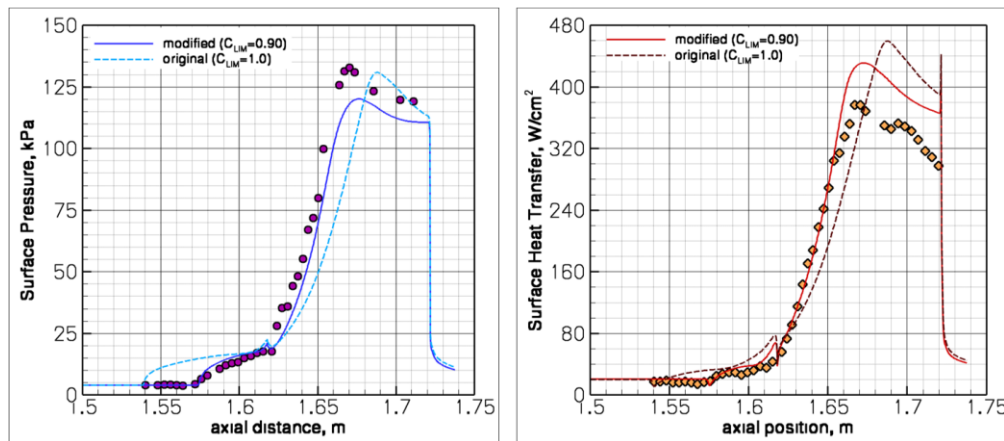

Figure 76: Comparison of Modified SST Model with Phase II Surface Measurements

However, using this approach to compute the flow over a large 6° cone flare configuration, we again showed significant discrepancy between theory and experiment as shown in Figure 77.
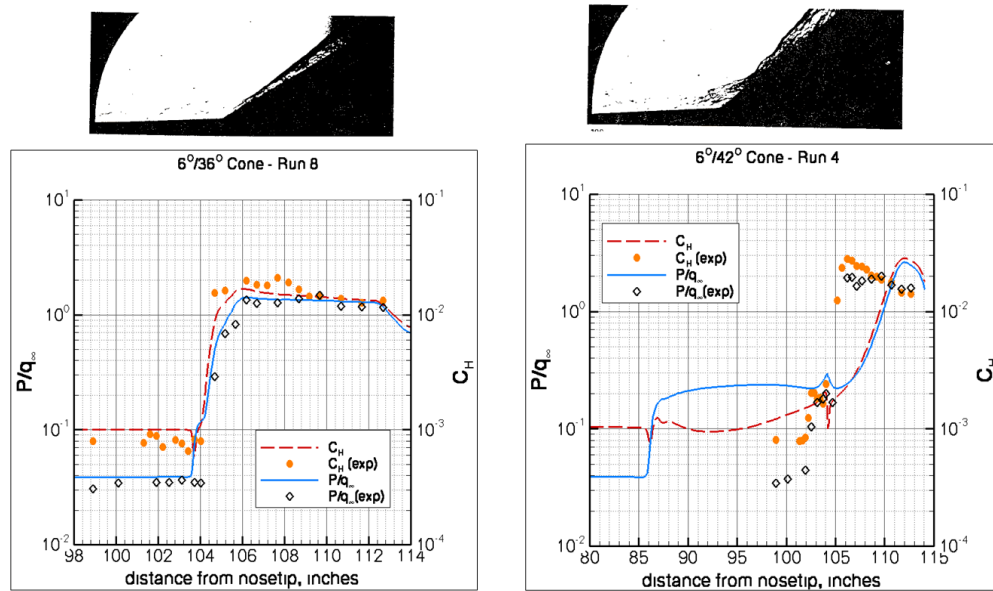
Figure 77: Comparison of 6° Cone Experiments and Menter SST Solutions for 36° and 42° Flare

Recently we have constructed new models and instrumentation to provide detailed measurements in regions of shock wave/boundary layer interaction at the cone/flare junction on the large cone/flare model shown in Figure 78. The model dimensions which are shown in Figure 79 were selected to obtain very large Reynolds numbers (up to 0.2 billion) to ensure that the flow was fully turbulent over almost the complete length along the 8 ft model. Although there are individual gages placed along the cone, most of the heat transfer and pressure instrumentation was concentrated around the cone/flare junction as illustrated in Figure 78. Measurements of the detailed distribution of surface pressure and heating were obtained at the three test conditions shown in Figure 79 to provide data at wall to stagnation temperature ratios of 0.2 and 0.6; the latter being for a fully duplicated velocity at Mach 6. We also ran an additional test case at significantly lower Reynolds numbers and a Schlieren photograph of the flow for this case is shown in Figure 78. Currently we plan not to publish the test data for the three high Reynolds number conditions prior to a "blind" validation exercise to be conducted in conjunction with research being sponsored by the Air Force Office of Scientific Research (AFOSR).
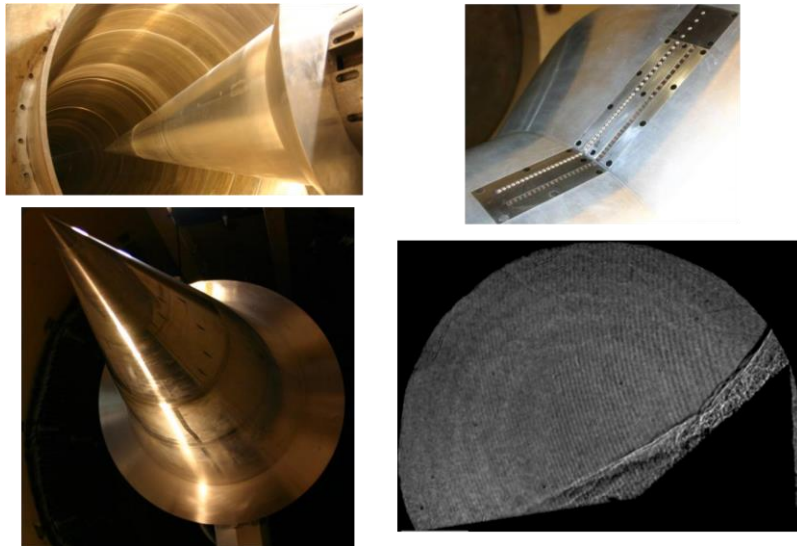
Figure 78: Code Validation Experiments for Blind Computation to Predict Hypersonic High Reynolds Number Turbulent Separated Shock Boundary Layer Interaction
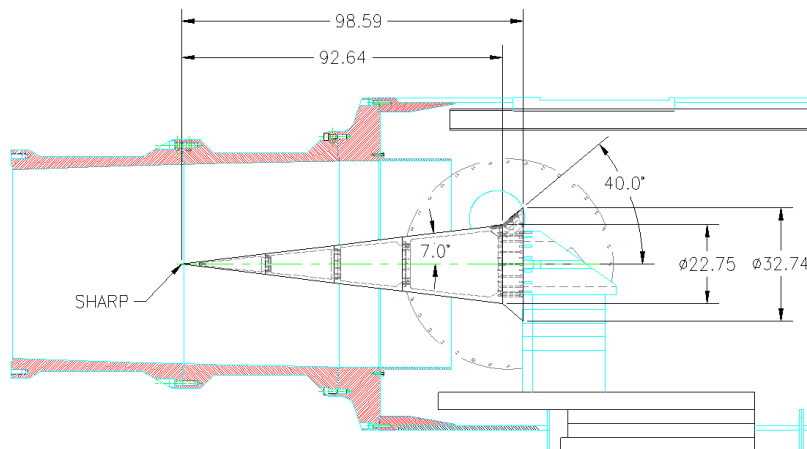
	Mach #	ReL	Tw/To
Condition A	6.0	0.4E8	0.6
Condition B	6.0	0.4E8	0.2
Condition C	6.0	0.2E9	0.6

Figure 79: Model Configuration and Test Conditions for "Blind Validation Study"

Currently we are preparing to produce additional code validation data in regions of attached and separated shock wave/turbulent boundary layer interaction using the hollow cylinder/flare configuration shown in Figure 80. We plan to obtain measurements on the surface and flowfield characteristics of the interaction regions in high Reynolds number flows for Mach numbers between 4.5 and 10 for a range of wall to freestream stagnation temperature ratios. This model would also be

modified to provide measurements in shock-induced separated flows and regions of flow separation in steps and cavities with a model which is illustrated in Figures 81, 82 and 83. High-frequency surface measurements will be made with thin-film platinum gages and strain-gage and piezoelectric pressure instrumentation. Flowfield measurements will be made with hot-wire probes and nonintrusive laser diagnostics. The measurements from these studies will be performed and released in two phases; the first will contain principally surface measurements with flowfield data provided by Schlieren and PLIF visualization. We will request pre-test computations which will be compared with the surface measurements in a "blind" validation exercise to be presented in an AIAA forum. For the second phase we will select specific model and flow geometries for which we will obtain detailed mean and fluctuating flowfield measurements with hot-wire and high-frequency laser diagnostics. We plan to compare these measurements in a second "blind" validation exercise to be presented at an AIAA meeting.
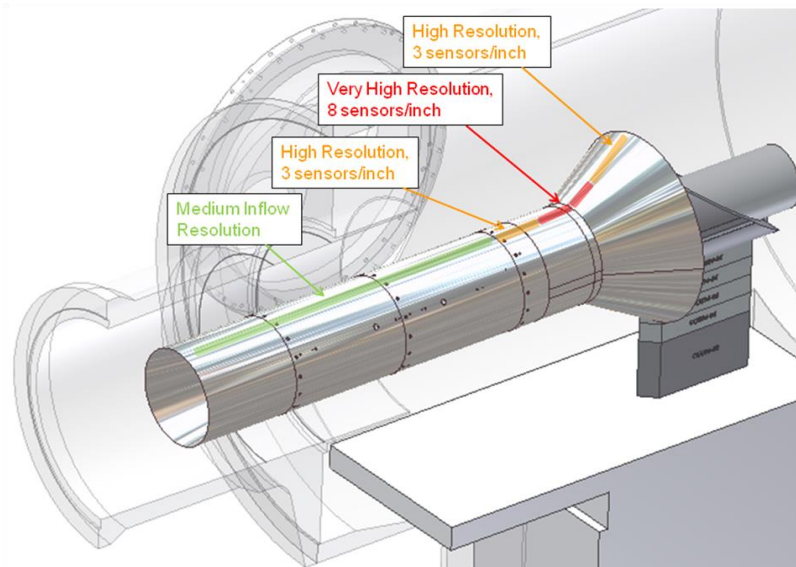

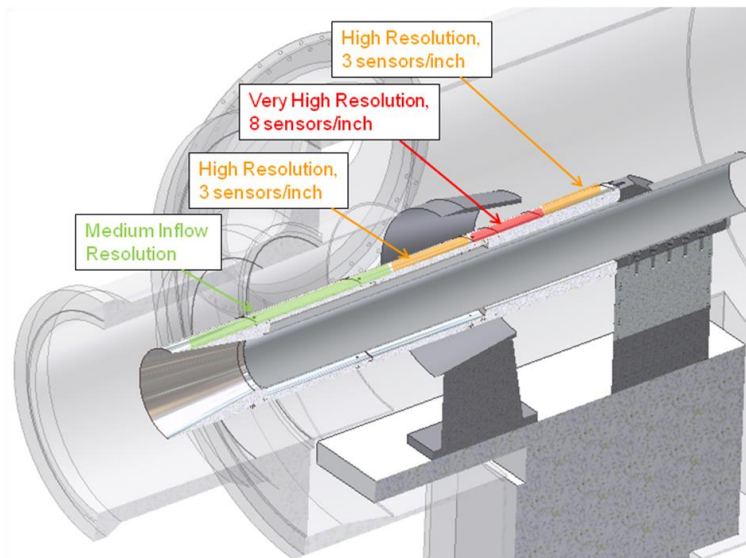**Figure 80: Large-scale Cylinder/Flare Model shown in LENS II Facility**

Figure 81: Large-scale External Shock Generator Model shown in LENS II Facility
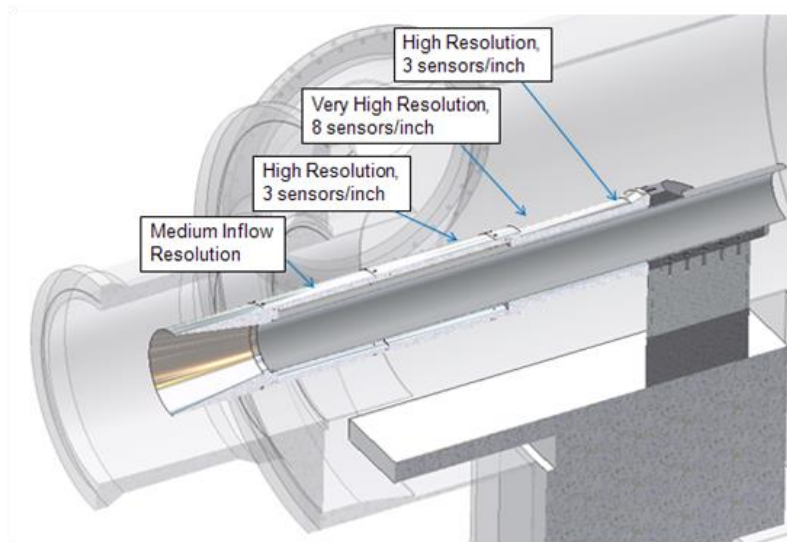
Figure 82: Large-scale Backward-facing Step Model shown in LENS II Facility
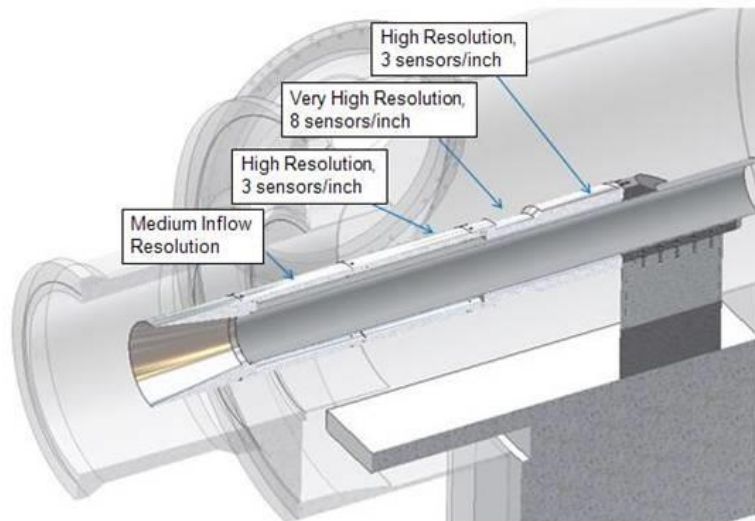
Figure 83: Large-scale Cavity Flow Model shown in LENS II Facility

5.0 STUDIES OF ROUGHNESS AND BLOWING EFFECTS ON BLUNT AND SLENDER HYPERSONIC VEHICLES

Over the past 30 years, we have been conducting experimental studies to examine the effects of surface roughness on the aerothermal characteristics of both nosetips and conical re-entry vehicles. These studies have included work to determine the enhanced heating and skin friction on spherical and ablated nosetip configurations and on slender ballistic and maneuverable re-entry vehicles as illustrated in Figure 84. In these studies we made measurements with rough surfaces constructed with the surface characteristics of sand-grain roughness and with a number of spherical and conical roughness shapes. Our goal in these studies and in continuing work with NASA and U.S. Air Force is to develop correlations and prediction methods to determine the skin friction and heating loads to a

surface of arbitrary geometry. We would also like to establish a reference geometry of surface roughness which is more easily defined and constructed than "sand-grain" roughness.

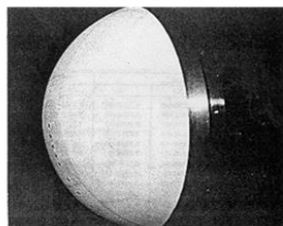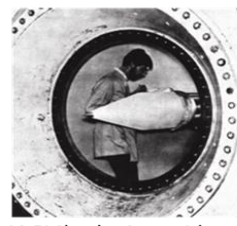Biconic Nosetip with Sand-Grain and Patterned Roughness

6° Slender Cone with Sand Grain and Patterned Roughness

Spherical Nosetip with Patterned Roughness

10.5° Slender Cone with Patterned Roughness and Surface Blowing

- Previous investigations focused on determining relationships between smooth surfaces, 'sand grain' roughness, and reproducible, patterned roughness geometries.

- Over 200 tests were performed for both blunt body and slender cone geometries.

- Variables included nose geometry, model incidence, and different roughness types, heights, shapes, and distributions.

- Goal is to develop an empirical correlation relating surface roughness characteristics (height, shape, spacing) to heat transfer augmentation rate.

Figure 84: Previous Roughness and Blowing Studies Performed at CUBRC

The models and instrumentation we are currently using in studies for NASA to develop accurate prediction techniques to design capsule heat shields are illustrated in Figure 85. In these studies we are investigating boundary layer transition and heating enhancement on spherical heat shield configurations constructed with both sand grain and patterned roughness. Measurements of roughness-induced heating enhancement for a range of roughnesses obtained in earlier AFOSR-sponsored studies are shown in Figure 86. Here we see the different trip geometries influence both the onset of transition and the enhanced heating levels. The magnitude of heating enhancement factor varies from 1.4 to 1.2 depending upon the location at which the measurements were made and the character of the surface roughness as illustrated in Figure 86. Figure 87 shows a correlation of the heating enhancement factor in terms of the reference Reynolds number and the effective sand-grain heating factor determined from a roughness shape parameter. Here it can be seen there is significant scatter in this correlation which in part reflects from the interaction between the roughness effects on boundary layer transition and the heating to the roughness elements with different geometric characteristics.

Erik Mundy's note: doesn't match Figure 86
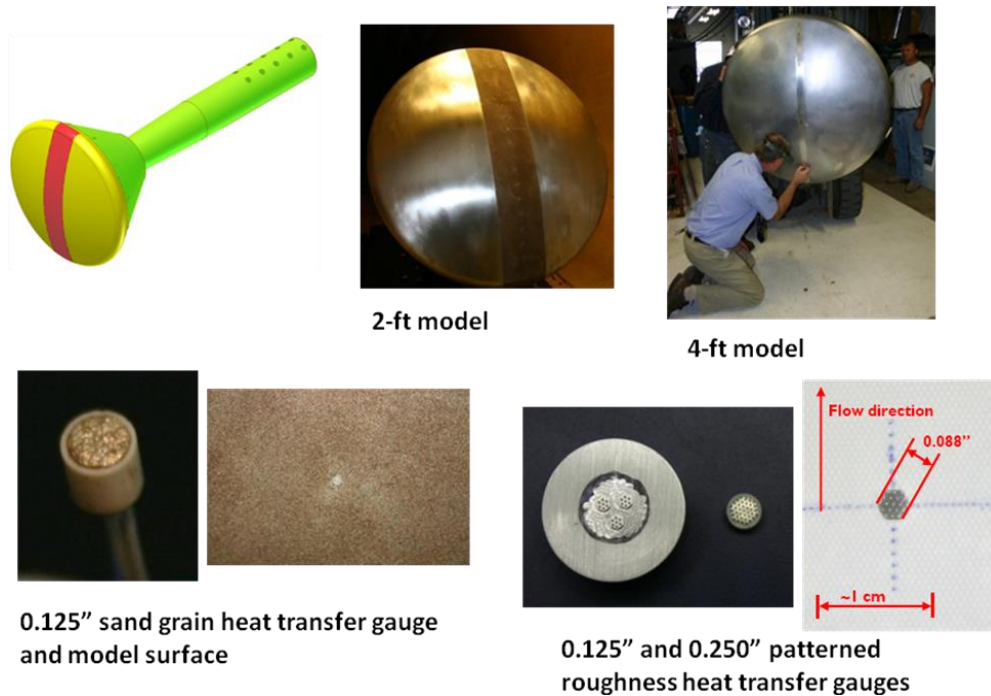
Figure 85: Models and Instrumentation Employed in Current Roughness Study of CEV Reentry Geometry
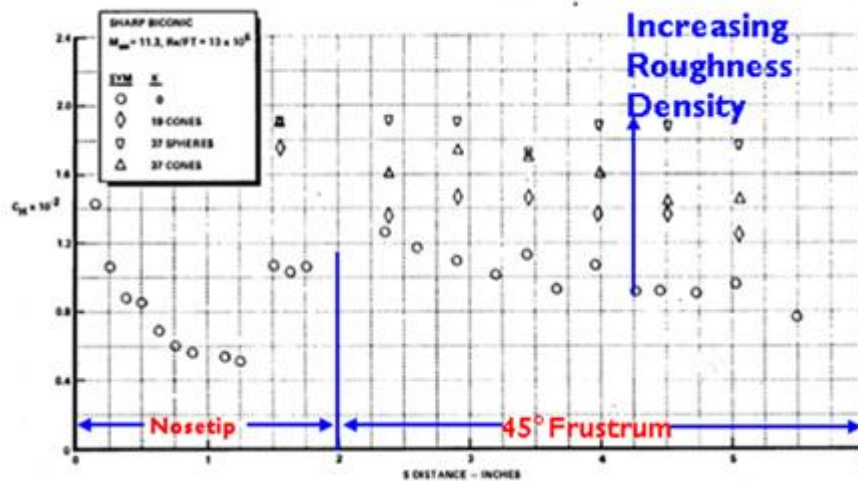
Figure 86: Roughness Geometries and Sample Heat Transfer Distributions
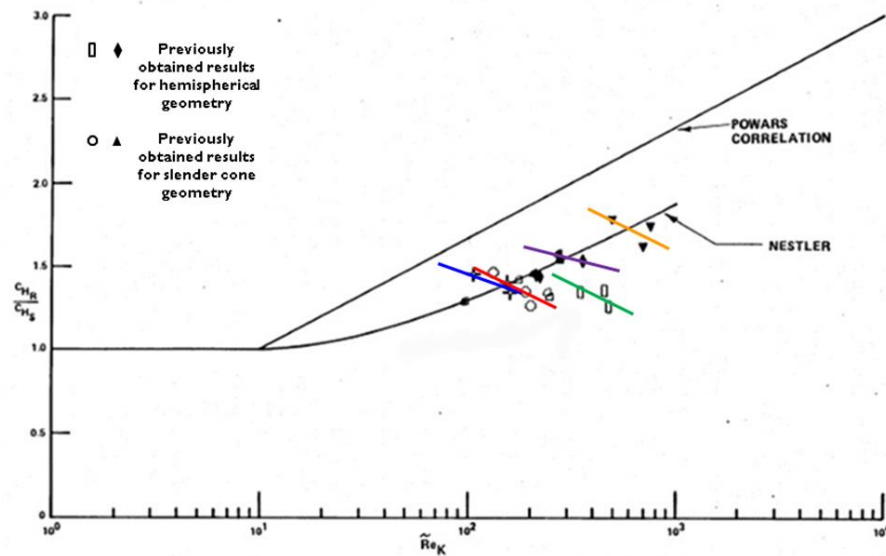
Figure 87: Roughness Correlations in Terms of Roughness Shape, Spacing, and Height with Roughness Reynolds Number

In a companion study, we are preparing models to examine the effect of combined roughness and blowing on the heating rates to nosetips and slender re-entry vehicles. Figure 88 shows both slender and blunt models constructed earlier with porous surfaces and we are using similar construction techniques to prepare the rough and blowing models of the CEV capsule for work we are performing with NASA.

Rough and Blowing Slender Cone   SCANT blowing hemisphere

Rough and Blowing CEV Reentry Vehicle
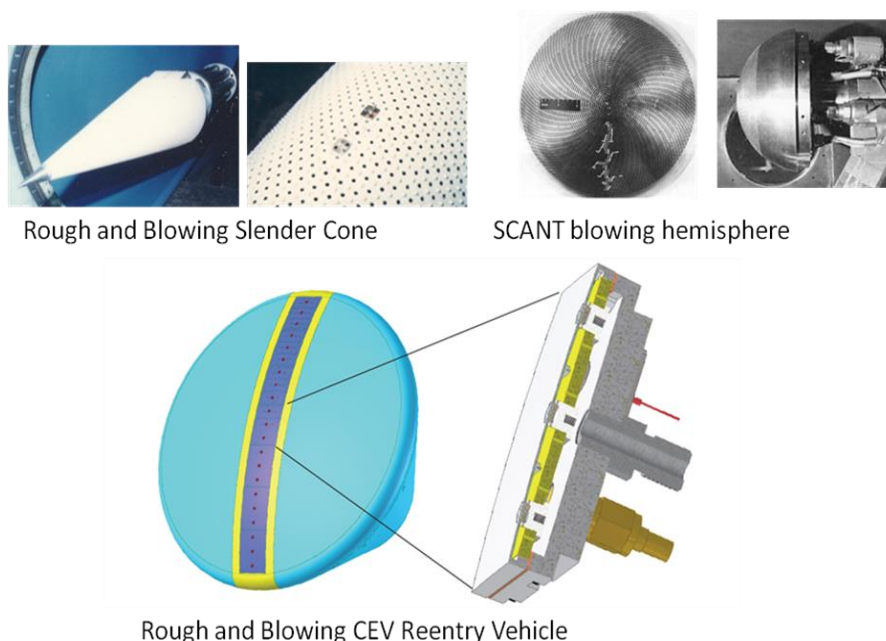
Figure 88: Previous Blowing Experiments Performed at CUBRC and Currently Planned CEV Roughness with Blowing Test

For the NASA program, we are constructing unique thin-film and calorimeter based heat transfer instrumentation to measure heating rates in the presence of surface blowing. In this work we employ a model with a well-defined surface and blowing geometry constructed with closely spaced spherical roughness elements as illustrated in Figures 89 and 90. These measurements will be later supplemented with flowfield data obtained with nonintrusive laser diagnostics and will form data sets with which to examine the separate and combined effects of surface roughness and blowing and the influence of boundary layer transition on these results.

Figure 89: Planned CEV Roughness with Blowing Test

Figure 90: Roughness with Blowing Heat Transfer Sensor

6.0 REAL GAS AND SURFACE CATALYSIS STUDIES IN THE LENS I AND XX FACILITIES

In the past seven years, there has been a major effort to perform experiments in the LENS I and XX facilities to evaluate the models describing real gas chemistry and the surface interaction effects associated with catalytic h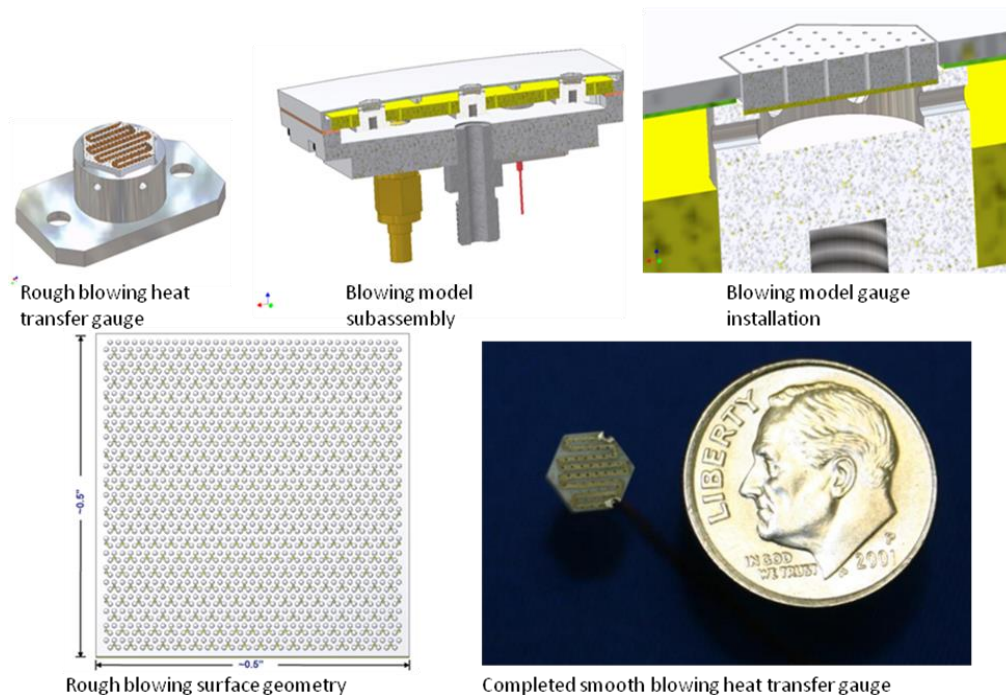eating. It has been these programs that have been the driver for developing the LENS XX expansion tunnel where we can generate velocities of up to 11 km/s (see Figure 91) where real gas effects in air and other test gas environments (see Figure 92) have major effects on the aerothermal loads experienced by capsules entering the earth's atmosphere and other planets such as Mars, Venus and Jupiter. A major objective for testing in the LENS XX facility within the next year is to duplicate the FIRE-II flight tests with a full-scale replica instrumented with similar spectrographic instrumentation. While we have experienced good success in predicting the flows in the LENS I reflected shock tunnel for total enthalpies of less than 5 MJ/kg for velocities of less than 3 km/s (see Figures 93 and 94), we have been unable to accurately predict translational temperatures or NO concentrations for total enthalpies of 10 MJ/kg or 4.5 km/s. For this 10 MJ/kg condition, measurements of velocity using a Doppler velocimeter are in excellent agreement with predictions indicating that the losses in total enthalpy are small. However, we failed to predict the translational temperature and concentration of NO with any degree of accuracy as shown in Figures 94 and 95.
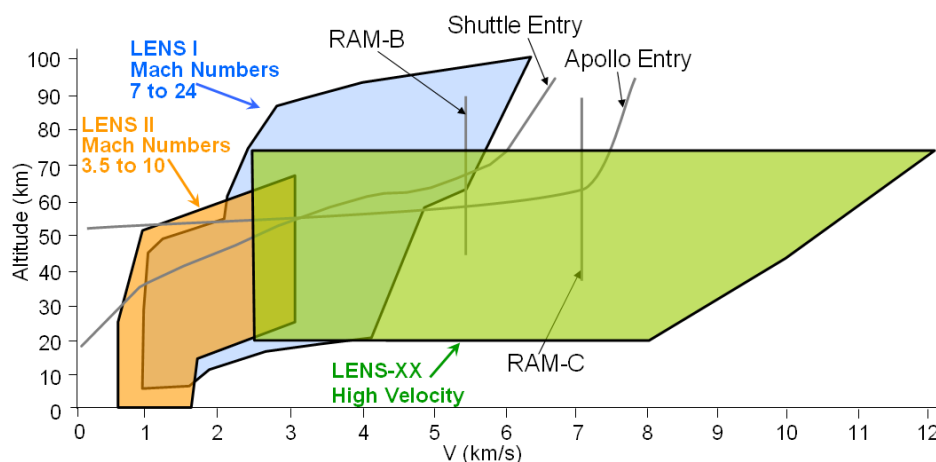
Figure 91: Velocity/Altitude Capabilities of LENS Reflected Shock and Expansion Tunnels

- Pure nitrogen (N2)
- AIR (N2/O2) *(Earth)*
- Carbon dioxide (CO2) *(Mars, Venus)*
- Hydrogen/helium (H2/He) *(Jupiter, Gas Giants)*
- Nitrogen/methane (N2/CH4) *(Titan)*
- Viitated Air (Air with CO2 and H2O addition)
- Noble gas (Ar/Ne/He mixtures)

Combinations of these or any other gases possible

Figure 92: Test Gas Environments for LENS Reflected Shock and Expansion Tunnels
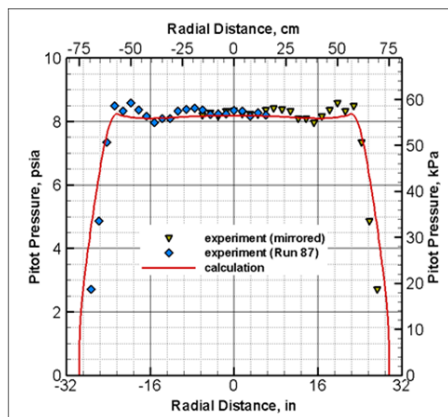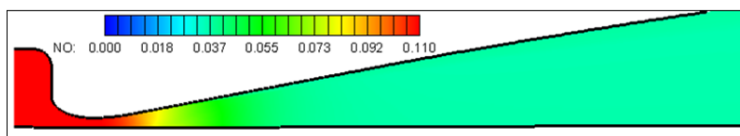
- 2D/Axisymmetric nozzle code (Candler 2005-5202)
- Full equilibrium computed in reservoir
- High-pressure, excluded volume equation of state
- Finite rate chemistry model 5-species air: N_2, O_2, NO, N, O (rates from Park-90 and/or Gri-Mech)
- Finite rate vibration relaxation, 1-SHO (rates computed by Millikan-White or Park-94)
- Vibration-dissociation coupling via Park T-Tv model
- Spalart-Allmaras turbulence model (Catris&Aupoix correction)

Figure 93: Computational Modeling of Reflected Shock Tunnel Nozzle Flow
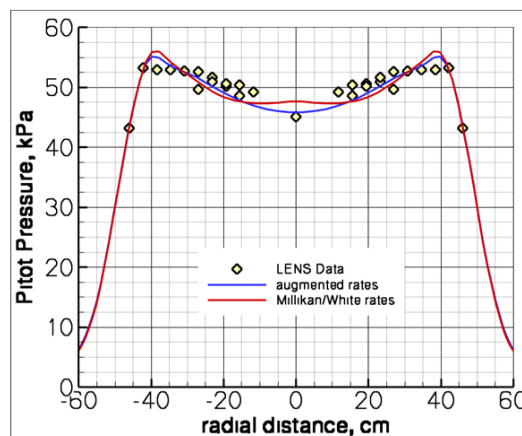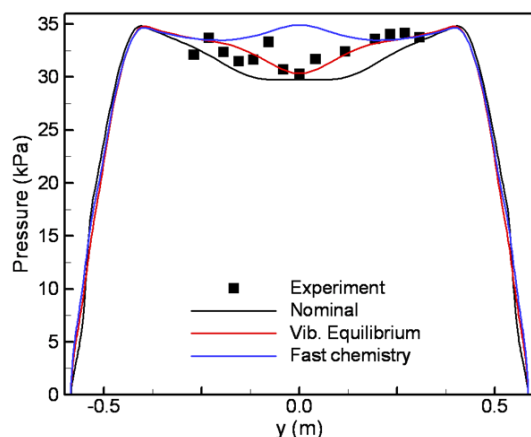
	U=3km/s (h_0 = 5 MJ/kg)			U=4.5km/s (h_0 = 10 MJ/kg)			U=6km/s (h_0 = 20 MJ/kg)		
	prediction	experiment	% diff	prediction	experiment	% diff	prediction	experiment	% diff
T_{TRANS}, K	221	200	11	563	270	109			
T_{ROT}, K	221	195	13					?	
y_{NO}				0.051	0.016	219			
U, m/s	3129	3092	1	4464	4581	3			

Figure 94: Computational Modeling of Reflected Shock Tunnel Nozzle Flow – Results Compared to Measurements

Figure 95: Nonintrusive Measurements Related to Real-gas Effects in LENS I Reflected Shock Tunnel Facility

In experiments to evaluate the real gas effects on the flow over Apollo-like capsules in the LENS I reflected shock tunnel, we can clearly see that although we can predict the shock shape and pressure distribution over the capsul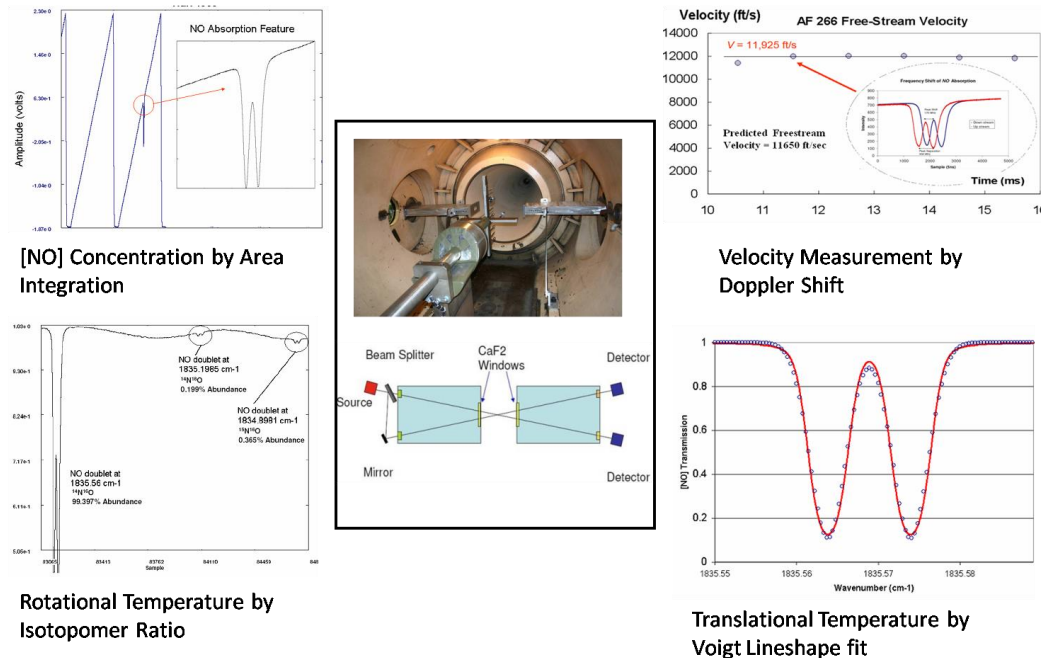e at angle of attack at total enthalpies of 5 MJ/kg, there are significant differences between predictions of shock shape and pressure distribution and experiment for the capsule at angle of attack for total enthalpies above 10 MJ/kg as shown in Figure 96. Plotting the pressure drop across the face of the capsule in ratio to the pitot pressure, we see that the prediction based on our current models of air chemistry (see Figure 97) is significantly different from the experimental data. However, questions remain as to whether this effect is related to inaccuracy in the tunnel test conditions or the models of flow chemistry in the shock layer. Similar questions arise from measurements of shock shape in a high-enthalpy CO_2 environment in the LENS reflected shock tunnel; however, because similar experiments in LENS XX are in good agreement with shock shape predictions, it is clear that nonequilibrium effects generated behind the reflected shock and persisting into the test section are a major reason for the discrepancy as shown in Figure 98.
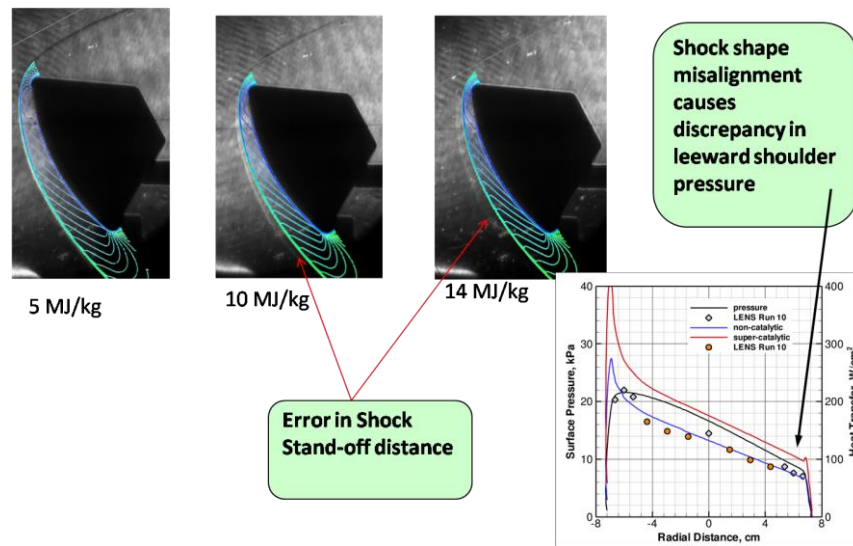
Figure 96: Real Gas Effects on Spherical Capsule Shock Layer Shape and Standoff Distance in Air
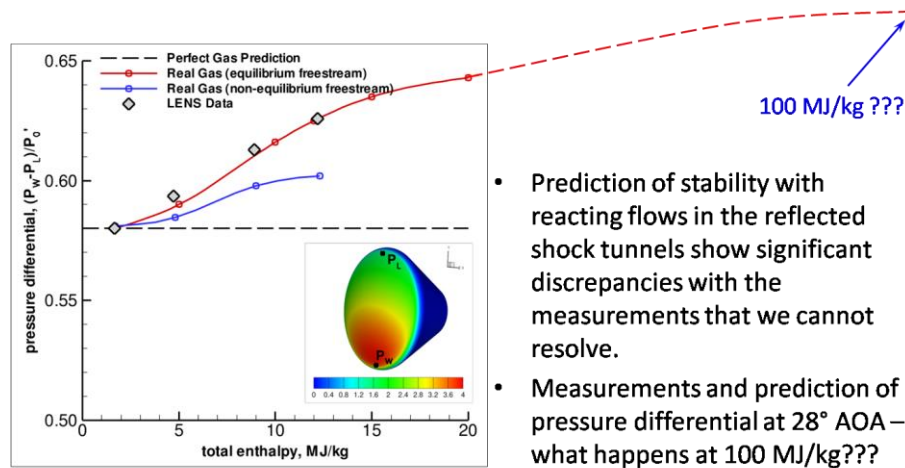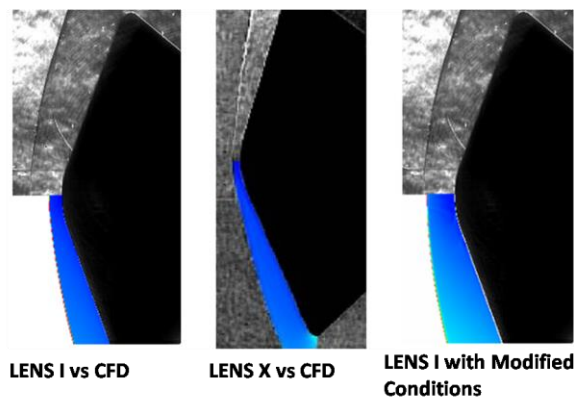

Figure 97: Real Gas Effects during Earth Entry on Vehicle Stability and Control

LENS I vs CFD   LENS X vs CFD   LENS I with Modified
                                              Conditions

- Studies in CO_2 have shown the sensitivity to shock shape (i.e. stability caused by thermal and chemical excitation) at even low enthalpies of 5 MJ/kg
- Current modeling "breaks-down" in predicting the thermochemical state of CO_2 in LENS I. By "fixing" the freestream conditions, we are able to match the distorted shock shape but the conventional modeling is wrong!
- Shock shape in LENS X looks good because it is a quiescent flowfield.
- CO_2 shows a level of thermal and chemical activity that is similar in magnitude to air at a much higher enthalpy level and may indicate what we will see at reentry velocities

Figure 98: Real Gas Effects on Shock Structure in CO_2 in Reflected Shock Tunnels and Expansion Tunnel

Similar studies have been conducted in air and nitrogen with a double cone configuration, the shock pattern over which and consequently the distribution of pressure, are strongly influenced by real gas effects. As before, predictions at the lower total enthalpies (3 MJ/kg) are in agreement with measurements; however, introducing real gas effects into the tunnel and shock layer flows using a reflected shock tunnel results in discrepancies between theory and experiment for both shock shape and pressure distribution as shown in Figure 99.

Why study the double cone?

- It is highly sensitive to real gas effects for high enthalpy real-gas effects.
- Complex interaction is very sensitive to numerics, physical modeling, grid resolution, and freestream conditions.
- Good agreement for low enthalpy, but we are still missing some modeling at 10 MJ/kg.

results 10MJ/kg   results 3MJ/kg
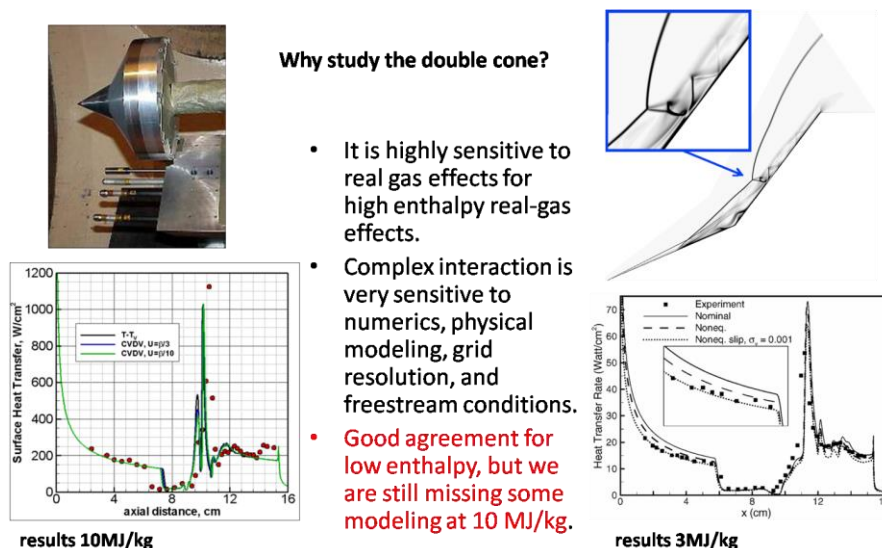
Figure 99: Real Gas Effects on Shock/Boundary Layer Interaction

Perhaps the most famous example of real gas effects on re-entry vehicles occurred on the space shuttle where the stability of the shuttle was significantly reduced by real gas effects. We simulated these conditions in the LENS I tunnel demonstrating that decrease in shuttle stability resulted principally from lower pressures on the wing rather than a decrease in flap effectiveness as shown in Figure 100.

- Flap force anomaly observed on STS-1 explained by comparing high enthalpy test results to cold flow measurements.
- Real-gas effects change the trim and stability of maneuvering vehicles
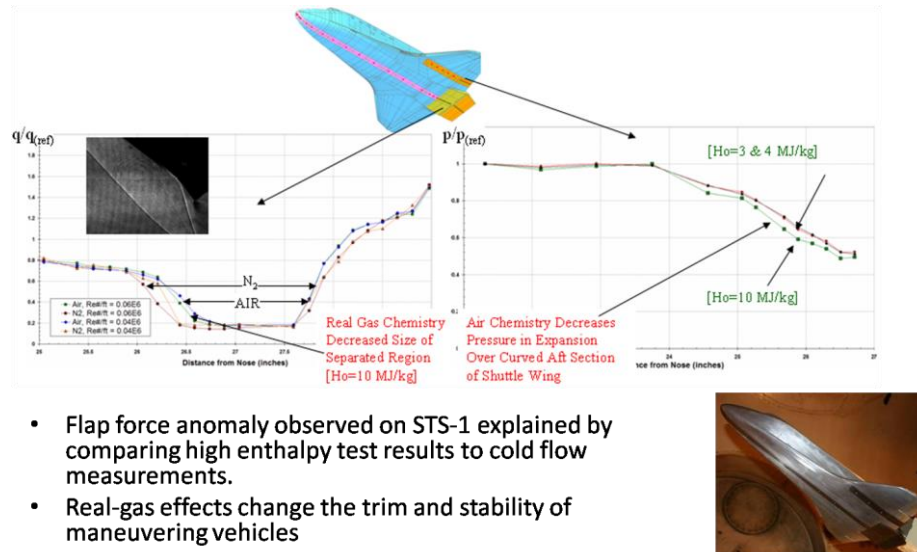
Figure 100: Real Gas Effects on Vehicle Stability and Control

The importance of real gas effects on the heating of re-entry vehicles was demonstrated in a number of our studies on blunt and slender re-entry vehicles (see Figure 101) tested in the LENS I facility. In many of our studies the best agreement between theory and experiment is obtained by assuming that the surfaces are "super-catalytic" with all the energy being combined on the surface with the measured design loads being twice those predicted for turbulent heating to the heat shield as illustrated in Figure 102.

Figure 101: Importance of Catalytic Heating Augmentation in Extrapolating Ground Test Aerothermal Measurements to Flight for Vehicle Design

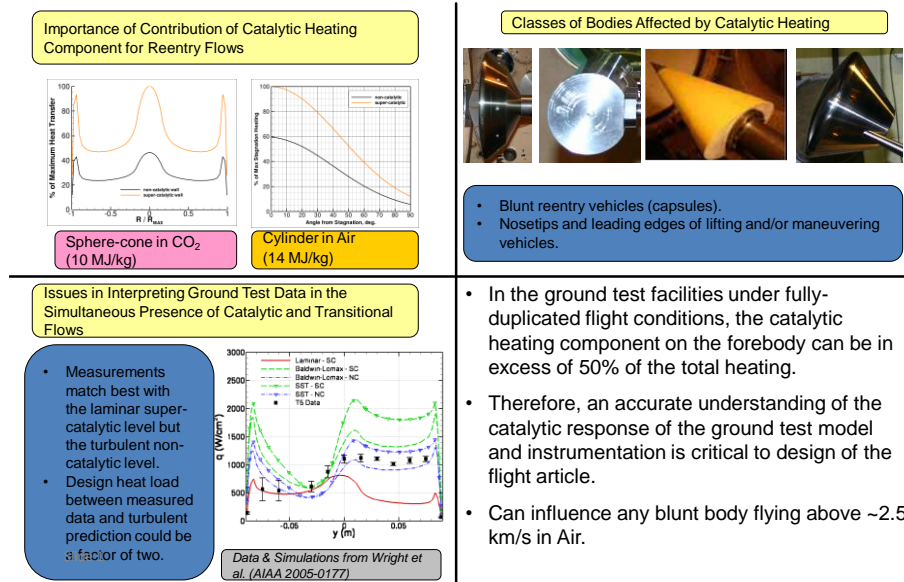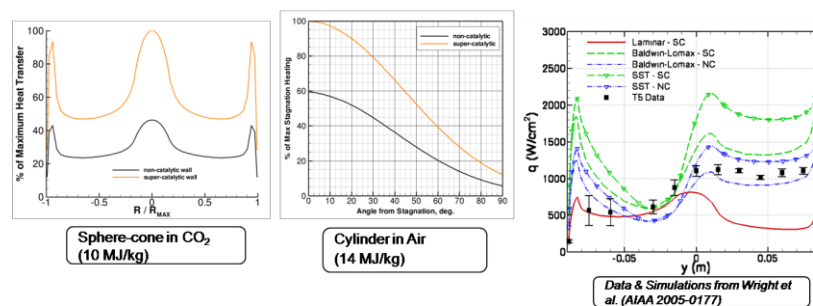- Measurements match best with the laminar super-catalytic level but the turbulent non-catalytic level.
- Design heat load between measured data and turbulent prediction could be a factor of two.

Figure 102: Importance of Catalytic Heating Augmentation in Extrapolating Ground Test Aerothermal Measurements to Flight for Vehicle Design

In studies of catalytic heating on heat shield shapes equipped with three different types of heat transfer instrumentation (thin film, silver slug calorimeter, and coaxial thermocouples), we found a surprising result that the heat transfer rate measured with each one of these different types of gages were in excellent agreement as shown in Figure 103. Similar results were obtained in further studies in nitrogen and CO_2 as shown in Figure 104. There remain serious questions as to whether these results are influenced by nonequilibrium in the freestream and therefore our additional work will be concentrated with measurements in the LENS XX tunnel.
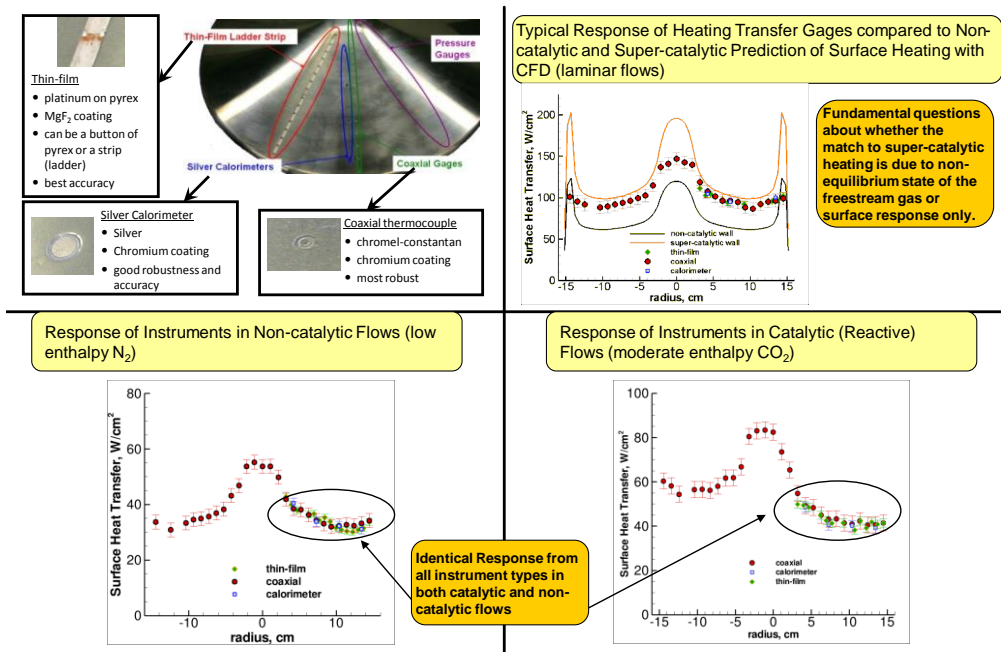
Figure 103: Measurement Techniques to Assess Catalytic Surface Response to Different Materials in Ground Test Facility
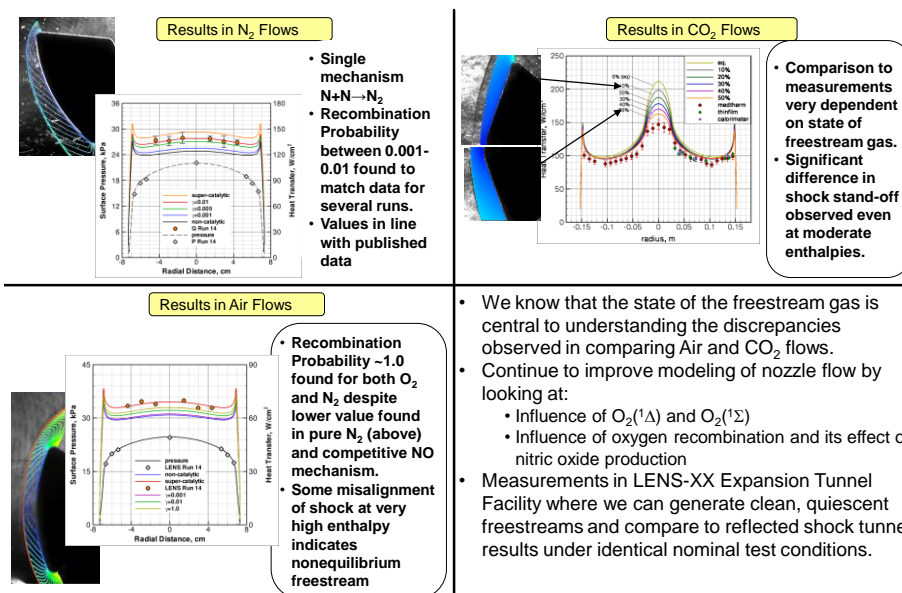

Figure 104: Results Obtained in N_2, Air, and CO_2 Flows in Catalytic Environments on Blunt Bodies and Future Work in this Area

BIBLIOGRAPHY

1. Holden, M.S. and Parker, R.A., "LENS Hypervelocity Tunnels and Application to Vehicle Testing at Duplicated Flight Conditions", Chapter 4, AIAA Publication *Advanced Hypersonic Test Facilities*, Frank K. Lu, Editor, published September 2002.

2. Holden, M.S, and Wadhams, T.P., "A Database of Aerothermal Measurements in Hypersonic Flows in 'Building Block' Experiments for CFD Validation," AIAA 2003-1137, 41st Aerospace Sciences Meeting and Exhibit, Reno, NV, January 6-9, 2003

3. Holden, M. S., Harvey, J., MacLean, M., Wadhams, T., Walker, B.J., "Development & Application of New Ground Test Capability to Conduct Full-Scale Shroud/Stage Separation," AIAA 2005-0696, 43rd AIAA Aerospace Meeting and Exhibit, Reno, NV, January 10-13, 2005.

4. Holden, Michael S., "Aerothermal and Propulsion Ground Testing that Can Be Conducted to Increase Chances for Successful Hypervelocity Flight Experiments", the von Karman Institute, October, 2005, Brussels, Belgium. To be published in RTO Course "Flight Experiments for Hypersonic Vehicle Development."

5. Holden, Michael S., Wadhams, Timothy P., Smolinski, Gregory J., MacLean, Matthew G., Harvey, John and Walker, Bill J., "Experimental and Numerical Studies on Hypersonic Vehicle Performance in the LENS Shock and Expansion Tunnels," AIAA 2006-0125, 44th AIAA Aerospace Sciences Exhibit & Meeting, Reno, NV, January 8-12, 2006.

6. Smolinski, Gregory J., Wakeman, Thomas R., and Holden, Michael S. "Experimental Aerodynamic Transport Characterization of Space Shuttle Debris using Stereogrammatics," AIAA 2006-0721, 44th AIAA Aerospace Meeting & Exhibit, Reno, NV, January 9-12, 2006.

7. Parker, Ronald A., Wakeman, Thomas, MacLean, Matthew and Holden, Michael, "Nitric Oxide Concentration Measurements with a Quantum Cascade Laser in the LENS I Hypersonic Shock Tunnel Facility," AIAA 2006-926, 44th AIAA Aerospace Meeting & Exhibit, Reno, NV, January 9-12, 2006.

8. Holden, Michael S., Wadhams, Timothy P., MacLean, Matthew, Parker, Ronald A., "Experiments in Numerical Studies of Low Density and Real Gas Effects on Regions of Shock Wave/Boundary Layer Interaction in Hypervelocity Flows," Report No. A-06-U-006, June 2006

9. Holden, Michael S., Wadhams, Timothy P., MacLean, Matthew, Mundy, Erik and Parker, Ronald, "Experimental Studies in LENS I and LENS X to Evaluate Real Gas Effects on Hypervelocity Vehicle Performance," AIAA 2007-204, 45th Aerospace Meeting & Exhibit, Reno, NV, January 8-11, 2007.

10. Holden, Michael, Wadhams, Timothy, MacLean, Matthew, and Walker, Bill J., "Experimental Studies in Hypersonic Flows for Facility and Code Validation," AIAA 2007-1304, 45th Aerospace Meeting & Exhibit, Reno, NV, January 8-11, 2007.

11. Nompelis, I., Candler, G., Holden, M. and MacLean, M., "Investigation of Hypersonic Double Cone Flow Experiments at High Enthalpy in the LENS Facility," AIAA 2007-203, 45th Aerospace Meeting & Exhibit, Reno, NV, January 8-11, 2007.

12. Parker, Ronald, Wakeman, Thomas, MacLean, Matthew and Holden, Michael, "Measuring Nitric Oxide Freestream Velocity using Quantum Cascade Lasers at CUBRC," AIAA 2007-1329, 45th Aerospace Meeting & Exhibit, Reno, NV, January 8-11, 2007.

13. MacLean, M.; Mundy, E.; Wadhams, T.; Holden, M.; Johnson, H.; Candler, G. "Comparisons of Transition Prediction using PSE-Chem to Measurements for a Shock Tunnel Environment." AIAA Paper 2007-4490. 37th AIAA Fluid Dynamics Conference & Exhibit, Miami, FL: 25 - 28 June 2007

14. Wadhams, T.P., Mundy, E., MacLean, M.G., Holden, M.S., "Pre-Flight Ground Testing of the Full-Scale HIFiRE-1 Vehicle at Fully Duplicated Flight Conditions, Part II," AIAA 2008-0639, 46th AIAA Aerospace Sciences Meeting and Exhibit, Reno, NV, Jan. 7-10, 2008.

15. Holden, M.S., Smolinski, G.J., Mundy, E., MacLean, M., Wadhams, T.P., Walker, B.J., "Experimental Studies for Hypersonic Vehicle Design and Code Validation of the Unsteady Flow Characteristics associated with "Free Flight" Shroud and Stage Separation, and Mode Switching," AIAA 2008-0642, 46th AIAA Aerospace Sciences Meeting & Exhibit, Reno, NV, Jan 7-10, 2008.

16. Holden, Michael S., Wadhams, Timothy P., MacLean, Matthew, "Experimental Studies in the LENS Supersonic and Hypersonic Tunnels for Hypervelocity Vehicle Performance and Code Validation," AIAA 2008-2505, AIAA Meeting, Dayton, OH, April 28-30, 2008.

17. Holden, Michael S., Smolinski, Gregory J., Mundy, Erik, MacLean, Matthew and Wadhams, Timothy P., "Full-Scale Tests of Inlet Starting, Mode Switching and Component Separation at Fully Duplicated Flight Conditions," JANNAF-1022, 30th JANNAF Meeting, Boston, MA, May 12-16, 2008.

18. Smolinski, Gregory J., Holden, Michael S., Wakeman, Thomas, and MacLean, Matthew, "Full-Scale Free Flying HyFly Shroud Ejection Test at Fully Duplicated Mach 4 Flight Conditions in the LENS II Test Facility," 30th JANNAF Meeting, Boston, MA, May 12-16, 2008.

19. Holden, M.S., Mundy, E.P., and Wadhams, T.P., "A Review of Experimental and Analytical Studies of Roughness, Blowing, and Roughness with Blowing on Hemispherical and Conical Shapes at High Mach Numbers," AIAA 2008-3907, 38th AIAA Fluid Dynamics Conference & Exhibit, Seattle, WA, June 23-26, 2008.

20. Holden, M.S., Wadhams, T.P., MacLean, M., Mundy, E., "Review of Studies of Boundary Layer Transition in Hypersonic Flows over Axisymmetric and Elliptic Cones conducted in the CUBRC Shock Tunnels," AIAA Paper 2009-0782, Orlando, FL, January 2009.

21. Holden, M., Mundy, E., Wadhams, T., and MacLean, M., "Boundary Layer Transition, Roughness and Blowing Effects on Aerothermal Characteristics of Hemispherical Heat Shields," AIAA 2010-1066, 48th AIAA Aerospace Sciences Meeting, Orlando, FL, January 4-7, 2010.

22. Wadhams, T., MacLean, M., and Holden, M., "A Review of Transition Studies on Full-Scale Flight Vehicles at Duplicated Flight Conditions in the LENS Tunnels and Comparisons with Prediction Methods and Flight Measurements," AIAA 2010-1246, 48th AIAA Aerospace Sciences Meeting, Orlando, FL, January 4-7, 2010.

23. Holden, M., Harvey, J., Wadhams, T., and MacLean, M., "A Review of Experimental Studies with the Double Cone Configuration in the LENS Hypervelocity Tunnels and Comparisons with Navier-Stokes and DSMC Computations," AIAA 2010-1281, 48th AIAA Aerospace Sciences Meeting, Orlando, FL, January 4-7, 2010.

24. Parker, R., Holden, M. and Wakeman, T., "Shock Front Radiation Studies at CUBRC," AIAA 2010-1370, 48th AIAA Aerospace Sciences Meeting, Orlando, FL, January 4-7, 2010.

25. MacLean, M., Dufrene, A., Wadhams, T. and Holden, M., "Numerical and Experimental Characterization of High Enthalpy Flow n an Expansion Tunnel Facility," AIAA 2010-1562, 48th AIAA Aerospace Sciences Meeting, Orlando, FL, January 4-7, 2010.